

# Elemental abundances in Milky Way-like galaxies from a hierarchical galaxy formation model

De Lucia, Gabriella; Tornatore, Luca; Frenk, Carlos S.; Helmi, Amina; Navarro, Julio F.; White, Simon D. M.

*Published in:*
Monthly Notices of the Royal Astronomical Society

*DOI:*
10.1093/mnras/stu1752



*Publication date:*
2014

Monthly Notices of the ROYAL ASTRONOMICAL SOCIETY

MNRAS **445,** 970–987 (2014) doi:10.1093/mnras/stu1752

# Elemental abundances in Milky Way-like galaxies from a hierarchical galaxy formation model

Gabriella De Lucia,[1⋆] Luca Tornatore,[1] Carlos S. Frenk,[2] Amina Helmi,[3] Julio F. Navarro[4] and Simon D. M. White[5]

[1] *INAF–Astronomical Observatory of Trieste, via G.B. Tiepolo 11, I-34143 Trieste, Italy*
[2] *Institute of Computational Cosmology, University of Durham, Science Laboratories, South Road, Durham DH13LE, UK*
[3] *Kapteyn Astronomical Institute, University of Groningen, PO Box 800, NL-9700 AV Groningen, the Netherlands*
[4] *Department of Physics and Astronomy, University of Victoria, Victoria, BC V8P 5C2, Canada*
[5] *Max Planck Institut für Astrophysik Karl-Schwarzschild-Str. 1, D-85741 Garching, Germany*

Accepted 2014 August 27. Received 2014 August 25; in original form 2013 September 18

## ABSTRACT

We develop a new method to account for the finite lifetimes of stars and trace individual abundances within a semi-analytic model of galaxy formation. At variance with previous methods, based on the storage of the (binned) past star formation history of model galaxies, our method projects the information about the metals produced by each simple stellar population (SSP) in the future. Using this approach, an accurate accounting of the timings and properties of the individual SSPs composing model galaxies is possible. We analyse the dependence of our chemical model on various ingredients, and apply it to six simulated haloes of roughly Milky Way mass and with no massive close neighbour at $z = 0$. For all models considered, the [Fe/H] distributions of the stars in the disc component are in good agreement with Milky Way data, while for the spheroid component (whose formation we model only through mergers) these are offset low with respect to observational measurements for the Milky Way bulge. This is a consequence of narrow star formation histories, with relatively low rates of star formation. The slow recycling of gas and energy from supernovae in our chemical model has important consequences on the predicted star formation rates, which are systematically lower than the corresponding rates in the same physical model but with an instantaneous recycling approximation. The halo that resembles most our Galaxy in terms of its global properties also reproduces the observed relation between the average metallicity and luminosity of the Milky Way satellites, albeit with a slightly steeper slope.

**Key words:** Galaxy: abundances – Galaxy: evolution – Galaxy: formation – Galaxy: stellar content – galaxies: dwarf.

## 1 INTRODUCTION

The distribution and amount of heavy elements in different baryonic components of the Universe depend strongly on the details of the physical mechanisms that regulate the evolution of baryons as a function of cosmic time (among recent studies, see e.g. De Lucia, Kauffmann & White 2004; Oppenheimer & Davé 2006; Tornatore et al. 2010). As a consequence, chemical abundance studies provide considerable information about the sequence of events that characterize the formation and evolution of galaxies and, more generally, on the relative importance of the various gas-dynamical processes that determine the observed cosmic evolution of baryons.

Two excellent examples of such an 'archaeological' approach applied to galaxy evolution studies are: inferences on the star formation history of elliptical galaxies and its dependence on the galaxy stellar mass (e.g. Worthey, Faber & Gonzalez 1992; Matteucci 1994; Thomas, Greggio & Bender 1999; Graves, Faber & Schiavon 2009), and chemical evolution studies aimed at constraining the formation history of different components of our Milky Way (see e.g. the classical review by Tinsley 1980; Matteucci 2008 and references therein). Both kinds of studies take advantage of the so-called $\alpha$-elements (these include O, Mg, Si, S, Ca, and Ti), and of their enhancements relative to Fe. $\alpha$-elements are released mainly by

⋆ E-mail: delucia@oats.inaf.it

supernovae type II (SnII), originating from massive progenitors with relatively short main sequence lifetimes (∼3–20 Myr). In contrast, the main contribution to the Fe-peak elements is given by SnIa, that are believed to originate from thermonuclear explosions of white dwarf (WD) stars whose progenitors have lifetimes ranging from ∼30 Myr up to several Gyr. Therefore, the [$\alpha$/Fe] abundance ratio can be used as a powerful diagnostic of the star formation history and/or of the initial stellar mass function (IMF; Tinsley 1979; McWilliam 1997).

During the last decades, accurate abundance measurements have been collected for a large number of individual stars in our Milky Way and in a number of the brightest satellites of the Local Group, as well as for thousands of nearby galaxies. A range of chemical elements have been measured in stars, in the cold interstellar gas, and in the hot intergalactic medium, back to an epoch when the Universe was only about one tenth of its current age. More and better data will come from ongoing and future observational programmes. The interpretation of this vast amount of data requires sophisticated chemical models, able to follow self-consistently the evolution of individual element abundances.

Unfortunately, most of the detailed chemical models mentioned above are not embedded in the framework of the currently favoured cosmological model for structure formation. In contrast, all theoretical models of galaxy evolution in a cosmological context have traditionally relied on an instantaneous recycling approximation (IRA). These methods include hydrodynamical simulations and semi-analytic models of galaxy formation. The former introduces an explicit treatment of gas physics in *N*-body simulations. In the second approach, the evolution of the baryonic component is modelled invoking 'simple', yet physically and observationally motivated 'prescriptions'. The basic assumption is that galaxies form when gas condenses at the centre of dark matter haloes. Star formation, feedback processes, chemical enrichment, etc. then take place according to analytical laws which are based on theoretical and/or observational arguments. Adopting this formalism, it is possible to express the full process of galaxy evolution through a set of differential equations that describe the variation in mass as a function of time of the different galactic components (e.g. stars, gas, metals), and that are coupled to the merger history of the dark matter haloes extracted from the *N*-body simulations (for a review, see e.g. Baugh 2006).

The situation has improved significantly in recent years with detailed chemical schemes being incorporated both in hydrodynamical simulations (Tornatore et al. 2004; Scannapieco et al. 2005; Wiersma et al. 2009; Few et al. 2012) and in semi-analytic models of galaxy formation (Nagashima et al. 2005; Cora 2006; Pipino et al. 2009; Arrigoni et al. 2010; Benson 2012; Yates et al. 2013).

In this paper, we present a new, fully self-consistent implementation of chemical enrichment within a semi-analytic model of galaxy formation, and apply it to *N*-body simulations of Milky Way-like haloes. The layout of this paper is as follows: in Section 2, we provide a brief description of the simulations used in our study, and summarize the relevant elements of the reference galaxy formation model. In Section 3, we discuss the main ingredients of our chemical evolution model, and describe in detail how we have updated our galaxy formation model to relax the IRA. In Section 4, we analyse the influence of the different model ingredients, and in Section 5 we discuss how the basic properties predicted by our model for simulated Milky Way-like galaxies are affected by using the updated chemical evolution scheme. In Section 6, we show our basic predictions for the chemical distributions of stars in the spheroid and disc of our model Milky Way-like galaxies, as well as for the mass–luminosity relation of satellite galaxies. Finally, we discuss our results and summarize our conclusions in Section 7.

**Table 1.** Basic numerical parameters of the simulations used in this study. The table lists: the simulation name, the particle mass ($m_{\rm p}$), the virial mass of the halo ($M_{200}$) and the corresponding virial radius ($R_{200}$). For all these simulations, the Plummer-equivalent gravitational softening length has been set to 65.8 pc.

| Name | $m_{\rm p}$ ($\rm M_\odot$) | $M_{200}$ ($\rm M_\odot$) | $R_{200}$ (kpc) |
|---|---|---|---|
| Aq-A-3 | $4.91 \times 10^4$ | $1.84 \times 10^{12}$ | 245.64 |
| Aq-A-2 | $1.37 \times 10^4$ | $1.84 \times 10^{12}$ | 245.88 |
| Aq-B-2 | $6.45 \times 10^3$ | $8.19 \times 10^{11}$ | 187.70 |
| Aq-C-2 | $1.40 \times 10^4$ | $1.77 \times 10^{12}$ | 242.82 |
| Aq-D-2 | $1.40 \times 10^4$ | $1.77 \times 10^{12}$ | 242.85 |
| Aq-E-2 | $9.59 \times 10^3$ | $1.19 \times 10^{12}$ | 212.28 |
| Aq-F-2 | $6.78 \times 10^3$ | $1.14 \times 10^{12}$ | 209.21 |

## 2 THE SIMULATIONS AND THE GALAXY FORMATION MODEL

In this paper, we make use of the simulations carried out within the Aquarius Project (Springel et al. 2008). A sample of six haloes of roughly Milky Way mass and with no massive close neighbour at $z = 0$ were selected from the Millennium II Simulation (Boylan-Kolchin et al. 2009). The haloes and their immediate environment were then re-simulated at higher resolution within the original periodic cube of side $100\,h^{-1}$ Mpc using the following cosmological parameters: $\Omega_{\rm m} = 0.25$, $\Omega_\Lambda = 0.75$, $\sigma_8 = 0.9$, $n = 1$, and Hubble constant $H_0 = 100\,h\,{\rm km\,s^{-1}\,Mpc^{-1}}$ with $h = 0.73$. The adopted value for the normalization of the power spectrum ($\sigma_8$) is consistent with *WMAP* first-year results, but is higher than more recent estimates. However, as shown in previous work (Wang et al. 2008; see also Guo et al. 2013), this will not affect the results of our galaxy formation model significantly.

The simulated Milky Way haloes have virial masses ($M_{200}$[1]) in the range 0.8–1.8 $\times\ 10^{12}\,\rm M_\odot$, broadly consistent with observational estimates for the Milky Way (Battaglia et al. 2005; Smith et al. 2007). Haloes were simulated at different levels of resolution with particle mass $m_{\rm p}$ ranging between $3.143 \times 10^6\,\rm M_\odot$ (for Aq-A-5) and $1.712 \times 10^3\,\rm M_\odot$ (for Aq-A-1). In the following, we will focus on the resolution level 2, which is available for all six Aquarius haloes. To verify the convergence of our physical model and to analyse the influence of different ingredients of the chemical model, we will also use a lower level of resolution for the Aq-A halo. This simulation (Aq-A-3) has been run with a dark matter particle mass $m_{\rm p} = 4.91 \times 10^4\,\rm M_\odot$, and a Plummer-equivalent gravitational softening length of 120.5 pc. Numerical parameters of all the simulations used in this work are summarized in Table 1.

Simulation data were stored for 111 (for Aq-F-2), 128 (Aq-B-2 to Aq-E-2), 512 (Aq-A-3), and 1024 (for Aq-A-2) snapshots. Each of these was processed using a standard friends-of-friends (FOF) algorithm with linking length equal to 0.2 times the mean inter-particle separation, and with the algorithm SUBFIND (Springel et al.

[1] In this study, $M_{200}$ is defined as the mass contained within the radius enclosing a mean density corresponding to 200 times the critical value at the redshift of interest.

2001) to identify all self-bound dark matter substructures in each FOF halo. Merger trees were then constructed linking each subhalo to a unique descendant in the subsequent snapshot (considering one every eight snapshots for Aq-A-2 and Aq-A-3, and all snapshots for the other Aq haloes) using software developed for the Millennium I simulation (for details, see Springel et al. 2005 and De Lucia & Blaizot 2007). A study based on the Millennium II by Boylan-Kolchin et al. (2010) has shown that the Aquarius haloes span the diverse properties of Milky Way haloes, in terms of assembly history and present day structure. Haloes A and C are found to have formed somewhat earlier than average. Halo F is somewhat unusual since it experienced a recent major merger, but it is found to be quite typical in most other properties.

The merger trees described above are used as input for a galaxy formation model. The specific model used in this work is the 'ejection model' described by Li, De Lucia & Helmi (2010). This is based on the model described in detail by De Lucia & Blaizot (2007, and references therein), but has been modified to follow more accurately processes on the scale of the Milky Way's satellites (for details, we refer to De Lucia & Helmi 2008 and Li et al. 2010). The same model has already been combined with the Aquarius dark matter simulations by Starkenburg et al. (2013) to investigate the properties of the satellites of Milky Way-like galaxies.

In our galaxy formation model, baryons are in four different components: stars in galaxies, cold gas in galaxy discs, hot gas associated with FOF haloes, and ejected gas that has been reheated and expelled outside haloes by Sn-driven winds. This ejected component can later be reincorporated into the hot gas component that is associated with the central galaxy of the FOF.

The circulation of baryons between different components is modelled using simplified yet physically and/or observationally motivated prescriptions. The chemical evolution model used in previous work tracked metal production in the IRA with a constant yield ($Y = 0.03\,\mathrm{M}_\odot$) of heavy elements for each solar mass of new stars, and a constant fraction ($R = 0.43$ for a Chabrier IMF) of stellar mass returned immediately to the interstellar medium. All material lost from stars was assumed to be perfectly mixed with the cold gas component, except in low-mass haloes ($\mathrm{M_{vir}} < 3 \times 10^{10}\,\mathrm{M}_\odot$) where it was assumed to be ejected directly into the hot gas component. Metals were exchanged between different baryonic phases according to specific feedback and reincorporation schemes. Generally, flows of metals were proportional to the mass flows between different baryonic components. For a detailed description of the scheme adopted to model chemical enrichment, we refer to De Lucia et al. (2004). In the next section, we describe how this model has been updated in order to account for the finite lifetime of stars and delayed gas recycling and chemical enrichment.

As for most published semi-analytic models, the morphological information for our model galaxies is given by the relative contribution of the 'disc' and the 'bulge'. The stellar disc component originates from quiescent star formation taking place in the gaseous disc forming following cooling of gas within the parent dark matter halo. In our previous work, the bulge component was assumed to form through both mergers and disc instability (see De Lucia & Helmi 2008 for details). An explicit modelling of the disc instability would be required to compare our model predictions with observational measurements of the 'bulge' of the Milky Way. The latter has a complex 3D structure that suggests that significant disc and/or bar dynamical evolution has taken place (e.g. Stanek et al. 1994; Dwek et al. 1995; Vásquez et al. 2013, and references therein). Unfortunately, however, the adopted modelling of disc instability is rather uncertain (see e.g. De Lucia et al. 2011 and references therein). In the following, we have decided to switch off this channel for (pseudo-)bulge formation. Therefore, our 'bulge' (spheroid) component should correspond to part of the Milky Way bulge and of its inner stellar halo. In addition, we do not model here the formation of the stellar halo from tidal stripping of satellites galaxies (as done for example in De Lucia & Helmi 2008 and Cooper et al. 2010 – this will be the subject of a future work), and do not distinguish between a thin and a thick disc component. Since the formation of the latter might be related to the formation of the stellar halo, and given it represents a small fraction (about 10–20 per cent) of the stellar mass in the disc, only comparisons between our model predictions and the thin disc are appropriate.

## 3 THE CHEMICAL EVOLUTION MODEL

During their lifetime, stars lose mass via stellar winds. Some stars ultimately undergo Sn explosions polluting the interstellar medium with both newly produced and earlier synthesized metals. The rates and time-scales of both these phenomena depend on the mass of the stars. In our previous work, we neglected the delay between star formation and the recycling of gas and metals. Our reference model was therefore not able to take into account the evolution of individual element abundances, and, in particular, did not describe well the production of elements around the iron-peak, which are mainly produced by SnIa with delay times ranging from a few tens of million years to several billion years. In this section, we describe how our earlier model has been updated to relax the IRA, and provide a more detailed and more realistic treatment of chemical evolution.

### 3.1 Basic equations and model ingredients

The rate at which enriched gas is lost by stars and Sne into the interstellar medium of a galaxy depends on the integral past star formation history of all its progenitors. At any given time $t$, the rate at which the element $i$ is injected into the interstellar medium can be calculated using the following equation:

$$R_{Z_i}(t) = R_{\mathrm{Ia}}(t) \cdot Q_i^{\mathrm{SnIa}} + \int_{M_{\mathrm{L}}}^{M_{\mathrm{SnII}}} \Psi(t - \tau_m) Q_i^{\mathrm{AGBs}}(m, Z) \phi(m)\,\mathrm{d}m + \int_{M_{\mathrm{SnII}}}^{M_{\mathrm{U}}} \Psi(t - \tau_m) Q_i^{\mathrm{SnII}}(m, Z) \phi(m)\,\mathrm{d}m. \quad (1)$$

In this work, we assume $M_{\mathrm{L}} = 0.1\,\mathrm{M}_\odot$, $M_{\mathrm{U}} = 100\,\mathrm{M}_\odot$ and $M_{\mathrm{SnII}} = 8\,\mathrm{M}_\odot$. The various terms in equation (1) represent the contribution of stars in different mass ranges. In particular:

(i) the first term represents the contribution from SnIa, and is the product between the rate of SnIa at time $t$ ($R_{\mathrm{Ia}}$ – see Section 3.1.1 for details), and the yields from SnIa ($Q_i^{\mathrm{SnIa}}$ – in our case, these do not depend on the metallicity or mass of the progenitors);

(ii) the second term represents the contribution of low-mass stars. Note that this integral extends to masses above the minimum mass of SnIa producing binary systems ($\sim 3\,\mathrm{M}_\odot$). Therefore, this term explicitly accounts for the ejection of metals during the asymptotic giant branch (AGB) phase of these stars, prior to the Sn explosions;

(iii) the last integral represents the contribution from stars with mass larger than $M_{\mathrm{SnII}}$, that end their life as SnII.

$\Psi(t)$ is the star formation rate at time $t$, $\phi(m)$ is the initial mass function, and $\tau_m$ is the lifetime of a star of mass $m$. The quantities $Q_i^{\mathrm{AGBs}}(m, Z)$ and $Q_i^{\mathrm{SnII}}(m, Z)$ represent the yields array for the

element $i$ from AGBs and SnII, and depend on the mass and the total metallicity of the star. In principle, our model can take into account the dependence on the detailed chemical composition of the stars so that the factors $\Psi(t-\tau_{\rm m})Q_i(m,Z)$ in the above equation should read as

$$\int \Psi(t-\tau_{\rm M}, Z_{1,...,{\rm N}})Q_i(m, Z_{1,...,{\rm N}})dZ_{1,...,{\rm N}}. \quad (2)$$

Since, however, we trace an average star formation event for each time-step, and the yields tables we employ depend only on the total metallicity, this double integral is not used in this work.

### 3.1.1 SneIa

To compute the first term of equation (1), it is necessary to know the rate of SnIa, which depends on the nature of the progenitor systems. Unfortunately, this is still poorly understood. The widely accepted scenario is that of a carbon and oxygen WD that accretes mass from a companion star in a binary system. As it approaches the Chandrasekhar limit ($1.4\,{\rm M}_\odot$), the highly degenerate WD ignites thermonuclear fusion in an explosive event that completely destroys the star (see e.g. Wang & Han 2012; Hillebrandt et al. 2013). One of the key unknowns is the nature of the companion star: another WD in the 'double degenerate model' (Iben & Tutukov 1984; Webbink 1984), a main sequence dwarf or an evolved giant in the 'single degenerate model' (Whelan & Iben 1973). Once the progenitor model is chosen, the SnIa rate can be computed by convolving the star formation rate with the distribution of the explosion times, that is usually referred to as 'delay time distribution' (DTD) function.

Recently, Greggio (2005, see also Ruiz-Lapuente & Canal 1998) has introduced a relatively simple and general analytical formulation for the SnIa rate that does not depend on the details of the progenitor model, and allows an efficient investigation of the influence of different distribution time delays (DTDs) on the chemical properties of interest. In this formalism, the rate of SnIa at an epoch $t$ can be written as

$$R_{Ia}(t) = k_\alpha \int_{\tau_i}^{\min(t,\tau_x)} A(t-\tau)\Psi(t-\tau){\rm DTD}(\tau){\rm d}\tau, \quad (3)$$

where $A(t-\tau)$ represents the realization probability of a given SnIa scenario from the stellar population born at the time $(t-\tau)$, $\tau_i$ is the minimum delay time and corresponds to the minimum evolutionary lifetime of the SnIa precursors, and $\tau_x$ is the maximum delay time. We assume $\tau_i = 29$ Myr (that is, in our formulation, the lifetime of a star with mass $8\,{\rm M}_\odot$) and $\tau_x = 20$ Gyr (the lifetime of a star with mass $0.8\,{\rm M}_\odot$). In chemical evolution models, $A$ is usually treated as a free parameter and is tuned to reproduce the present time SnIa rate. In our study, we will also treat $A$ as a free parameter, but will tune its value by considering the [Fe/H] and [O/Fe] distributions of disc stars for our model Milky Way galaxies.

The DTD is defined in the range $[\tau_i, \tau_x]$, and is normalized as

$$\int_{\tau_i}^{\tau_x} {\rm DTD}(\tau){\rm d}\tau = 1; \quad (4)$$

$k_\alpha$ is the number of stars per unit mass in a stellar generation and is derived from the IMF:

$$k_\alpha = \int_{M_{\rm L}}^{M_{\rm U}} \phi(m){\rm d}m \quad (5)$$

Therefore, equation (3) allows us to include consistently the SnIa events in our galaxy formation model by specifying the parameter $A$ and the DTD, and ignoring modelling details of the binary population of SnIa progenitors.

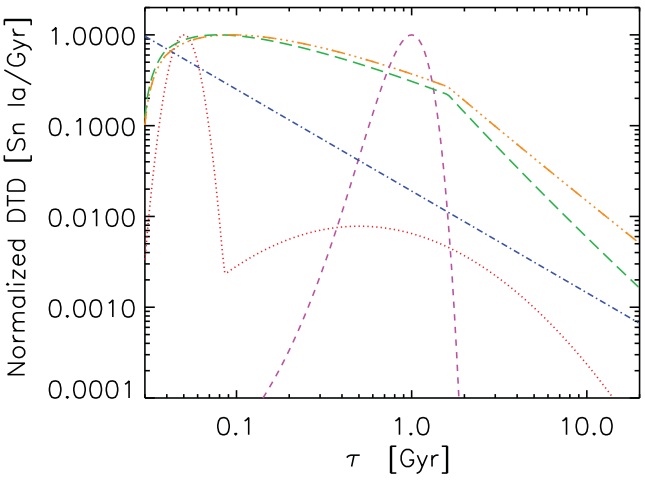


**Figure 1.** The normalized DTDs considered in this study (see text for details). The blue dot–dashed line corresponds to a power-law DTD with slope −1.12, as proposed by Maoz et al. (2012); the magenta dashed line to the narrow Gaussian DTD proposed by Strolger et al. (2004); the red dotted line to the bi-modal DTD proposed by Mannucci, Della Valle & Panagia (2006); the green long dashed and orange triple dot–dashed lines to two different variations of the DTD corresponding to a single degenerate scenario as described in Matteucci & Recchi (2001) and Bonaparte et al. (2013).

Formally, stars that end their life as SnIa should not be counted in the second and third terms of equation (1). However, in the adopted formalism for SnIa, the information on the mass distribution of these stars is hidden in the parameter $A$, and should be computed explicitly for each specific model corresponding to the assumed DTD. It is, in general, not possible to relate the $A$ parameters computed for different scenarios, as done for example by Arrigoni et al. (2010). Since the expected values for $A$ are typically small, below a few per cents, the correction would not influence significantly the chemical enrichment calculations. Therefore, in the following, we do not correct the second and third terms in equation (1).

### 3.1.2 The distribution function of the delay times for SneIa

As explained in the previous section, different progenitor scenarios for SnIa predict different distribution functions for their delay times. Different functions have been proposed in the literature, and below we will analyse the influence of five different DTDs.

(i) A power-law DTD with slope −1.12, as proposed by Maoz, Mannucci & Brandt (2012). This is shown as a blue dot–dashed line in Fig. 1, and has been inferred from a sample of 132 SneIa discovered by the Sloan Digital Sky Survey II in about 66 000 galaxies, with star formation histories reconstructed from the observed spectra. This DTD is consistent with the $\sim t^{-1}$ form that is generally expected in the double degenerate scenario.

(ii) The narrow Gaussian DTD function from Strolger et al. (2004). This has been measured from deep *Hubble Space Telescope* observations of 42 SneIa in the redshift range $0.2 < z < 1.6$. The analysis by Strolger et al. shows that delay time models that require a large fraction of 'prompt' Sne (in the work by Strolger et al., all SnIa explosions with delay times less than ∼2 Gyr) poorly reproduce the observed redshift distribution, and are rejected at high confidence level. The best fit to the observed data is obtained for mean delay times in the range 2–4 Gyr. The corresponding DTD is shown as a magenta dashed line in Fig. 1.

(iii) The bi-modal DTD proposed by Mannucci et al. (2006). This has been shown to simultaneously reproduce the SnIa rate evolution as a function of redshift, the dependence of the SnIa rate on host galaxy colours, and the increase of SnIa rate in radio-loud ellipticals. The assumption of this particular DTD implies that 30 to 50 per cent of the SneIa explode within $10^8$ yr from the star formation episode (the 'prompt' component), while the rest have delay times up to several Gyr (the 'tardy' component). To implement this particular DTD in our model, we use the analytic approximation presented in Matteucci et al. (2006). This is shown as a red dotted line in Fig. 1 and corresponds to a prompt component of ∼49 per cent.

(iv) Finally, two slightly different variations of the DTD corresponding to the single degenerate scenario, as described in Matteucci & Recchi (2001) and Bonaparte et al. (2013). The corresponding DTDs are shown by the green long-dashed and orange triple dot–dashed lines in Fig. 1 (we will refer to these as 'SD narrow' and 'SD broad', respectively). In these particular models, the fraction of Sne exploding within $10^8$ yr is of the order of ∼5 per cent, while the corresponding fraction within $4 \times 10^8$ yr is ∼23 per cent for the SD narrow DTD and ∼28 per cent for the SD broad DTD.

#### 3.1.3 Initial mass function and stellar lifetimes

In order to solve equation (1), one needs to define two additional quantities: the IMF that sets how newborn stars are distributed as a function of their stellar mass, and the typical lifetime for a star of given mass. In this work, we adopt a Chabrier IMF (Chabrier 2003), that is also consistently used to compute the luminosities of our model galaxies.

For the stellar lifetimes, we assume

$$\tau(m) = 1.2 \times m^{-1.85} + 0.003$$

for stars with mass $>6.6\,\mathrm{M}_\odot$, and

$$\tau(m) = 10^{\left[1.338-\sqrt{1.790-0.2232\times(7.764-\log(m))}\right]/0.1116-9}\,\mathrm{Gyr}$$

for stars with mass $\leq 6.6\,\mathrm{M}_\odot$ (see Padovani & Matteucci 1993, and references therein). We have also tested the different formulation presented in Maeder & Meynet (1989) and found that this ingredient of the chemical evolution model does not influence significantly the results discussed in this paper. As discussed in Romano et al. (2005), different stellar lifetime prescriptions differ mostly in the low stellar mass range. Therefore, models adopting different prescriptions for the stellar lifetimes differ mostly in the predicted evolution for species originating mainly from low-mass stars like $^3$He and $^7$Li. We have neglected here the metallicity dependence of stellar lifetimes that is, however, not very strong (Portinari, Chiosi & Bressan 1998, see also fig. 1 in Yates et al. 2013).

#### 3.1.4 Chemical yields

Stellar yields define the amount of material that is returned to the interstellar medium in the form of newly produced elements during the entire stellar lifetime, and represent one of the most important ingredients of any chemical evolution model. Different sets of yields are currently available, from state-of-the-art stellar evolution and nucleosynthesis calculations. Unfortunately, given the large uncertainties still affecting these studies, the available yields differ significantly from each other. This implies that chemical evolution models assuming different sets of yields can provide significantly different results, even when the same star formation history and initial mass function are assumed.

In a recent study, Romano et al. (2010) have tested different stellar nucleosynthesis prescriptions in the framework of a chemical evolution model of the Galaxy. They show that large uncertainties are still found, in particular for the majority of the iron-peak elements but also for more abundant species like carbon and nitrogen. Uncertainties originate from e.g. neglecting stellar rotation, different rates of stellar mass-loss, different treatment for convection, etc.

Our reference chemical model uses the following set of yields for stars in different mass ranges:

(i) Karakas (2010) for low- and intermediate-mass stars;
(ii) Thielemann et al. (2003) for SneIa;
(iii) Chieffi & Limongi (2004) for SneII.

Note that the yields by Chieffi & Limongi (2004) are defined for stellar masses between 13 and 35 $\mathrm{M}_\odot$. For stellar masses between 8 and 13 $\mathrm{M}_\odot$, we scale the yields proportionally to the stellar mass, while for more massive stars we use the values corresponding to the highest stellar mass tabulated. Below, we also test the influence of alternative sets of yields. In particular, we use the yields by van den Hoek & Groenewegen (1997) for low- and intermediate-mass stars, and those from Woosley & Weaver (1995, their case B) for SneII.[2] New sets of stellar yields have been recently calculated for low to massive stars using the same nuclear reaction network (Pignatari et al. 2013). It will be worth testing the influence of these new yields in the context of galaxy formation models like the one presented in this study.

### 3.2 Implementing chemical evolution in a galaxy formation model

Implementing equation (1) in the framework of our galaxy formation model is, in principle, straightforward. Each star formation episode could be treated as a simple stellar population (SSP) so that an accurate treatment of chemical evolution would simply require to store the information relevant to each star formation event, along with any parameter that might be useful to describe the future evolution of the SSP (e.g. its chemical composition or some proxy of it, the IMF in case it is assumed to depend on some physical condition of the gas, etc.). In practice, however, this approach is unfeasible because of the very large memory requirement implied.

#### 3.2.1 Storing the past average star formation history

One obvious possible approach to reduce the memory load is to rebin the past star formation history of each galaxy (and eventually of its different components) in a number of steps smaller than the actual number of time-steps used in the galaxy formation model. One can then use the stored information to compute the metal restitution rates at any time during model integration. This is the approach that has been adopted traditionally in semi-analytic models that include a detailed chemical evolution model (Nagashima et al. 2005; Arrigoni et al. 2010; Benson 2012; Yates et al. 2013).

When accounting for the contributions from both short-living (i.e. SneII) and long-living stars (i.e. SneIa and asymptotic giant branch stars – AGBs), the time interval of interest is comparable to

[2] When testing the yields by Woosley & Weaver (1995), we accounted for the contribution of radioactive $^{56}$Ni to Fe in stars with mass larger than $12\,\mathrm{M}_\odot$.

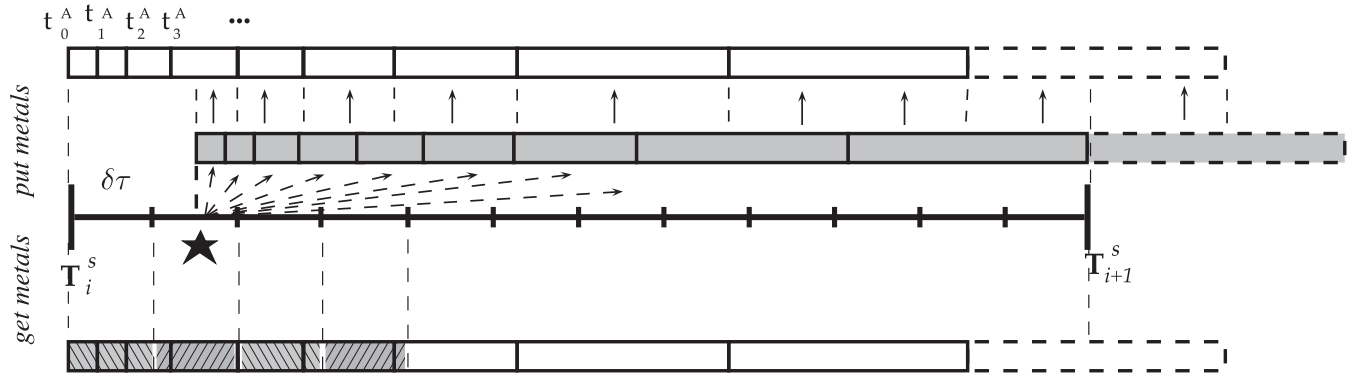


**Figure 2.** Schematic illustration of the method adopted to store the contributions from different types of stars in the future, and incorporate the metals in the baryonic gaseous phase of model galaxies during their evolution. The thick line shows the time interval between two subsequent snapshots. The two arrays at the top and at the bottom of the figure represent a 'metal restitution array' (RETURNEDMET) that is associated with each model galaxy and contains the mass of elements returned, at any time in the future, by the SSPs that constitute the model galaxy under consideration. At each time-step, the code computes the elements produced and adds them to the future bins (in case there is an episode of star formation), and then reads from the array RETURNEDMET the amount of metals that needs to be re-incorporated. The grey array shown in the figure is a 'virtual array' used to project metals in the appropriate bins.

the lifetime of the Universe. Since, however, most of the metals are produced by SneII and by the first SneIa, it is convenient to use a finer time resolution close to each star formation event. In practice, each galaxy is associated with an array carrying the information relative to the mass of stars formed and the metallicity of the cold gas at the time of the star formation event. These quantities might not be stored in a linear time grid: one can use, for example, an 'age grid' where the first bin represents $t = t_{\rm now}$ and the size of the bins increases as one moves to older ages (see e.g. appendix of Arrigoni et al. 2010 and section 5.1 of Yates et al. 2013; in the latter study, the time-bins are chosen to coincide with the internal time-steps of the galaxy formation code, and are set by the available snapshots of the background simulation).

As the galaxy evolves in time, the information stored in closer (and finer bins) need to be pushed to older ages, so that each entry of the array stores the average galaxy star formation rate in the time interval of the past it refers to. All the parameters needed to describe the evolution of the SSP will also be averaged so that each entry of the star formation array stores an *effective* SSP. Although it is reasonable to assume that star formation events close in time will not be significantly different in terms of the corresponding physical properties (e.g. metallicity), as soon as the time difference between the star formation events gets larger, the averaging will involve increasingly physically different SSPs. In addition, the stars ending up in a model galaxy, will generally form in several progenitors. By summing up the star formation histories corresponding to each progenitor, one will necessarily mix populations of intrinsically different metallicity. Since the calculation of the metal production depends on the age and metallicity of the SSPs, these averaging processes will mostly affect the contribution from long-living stars, whose accounting was the main reason to implement a non-IRA algorithm in the first place.

### 3.2.2 *Projecting metal restitution rates into the future*

An alternative approach, that we develop in this study, is to compute the metal ejection rates every time new stars are formed, and store the corresponding information *in the future*. As time proceeds, one can evaluate when/if the appropriate delay times have elapsed and, in that case, incorporate the stored metals in the baryonic phases of the model galaxies. Using this approach, an accurate accounting of the timings and properties of the SSPs is possible.

In practice, each model galaxy is associated with a 'metal-restitution array' that contains the mass of every element that will be returned, at some time in the future, by the SSPs that constitute the galaxy under consideration. The array will move forward in time as the galaxy evolves, so that also in this case it is necessary to perform some re-binning. The approximation we make is that the ejected metals are distributed uniformly in the corresponding time bins in the future. The total amount of metals formed is, however, computed using the exact times when new stars are formed, and the correct properties of the interstellar medium at the time of star formation (not averaged, as in the method illustrated in the previous section). In the following, we detail our practical implementation of the method summarized above.

To follow the abundance evolution of $n_{\rm met}$ elements, we attach to each galaxy an array (that we will call RETURNEDMET in the following) of $n_{\rm bins}$ bins, spanning the time range from $t = t_{\rm now} = 0$ to 14 Gyr in the future. Each time entry of RETURNEDMET is an array itself with room for $n_{\rm met} + 2$ elements. The two extra elements are used to store the amount of returned H + He, and the energy released by both SnII and SnIa explosions. The latter is used self-consistently to model the feedback from Sne (see below).

Our default option for the time-bins is that of using bins varying in such a way that each contains the same number of Sn events. Our reference runs adopt a total of 30 bins to follow the chemical evolution. As we will discuss below, we have verified that our results converge increasing the number of time-bins. We have also verified that our results are stable against alternative options for time-bins (e.g log-spaced or just fixed 'by hand').

The differential equations governing the evolution of each galaxy are solved dividing the time interval between two subsequent snapshots ($\Delta T^S = T^S_{i+1} - T^S_i$) in NSTEPS = 20. Let us indicate with $\delta\tau$ this internal time-step of galaxy evolution. The approach we adopt is illustrated in Fig. 2. The thick line shows the time interval between two subsequent snapshots and, in the example illustrated, a star formation episode occurs during the second integration time-step. The initial time of the array RETURNEDMET coincides with the initial time of integration $T^S_i$, and has a binning that is independent of that used to model galaxy evolution.

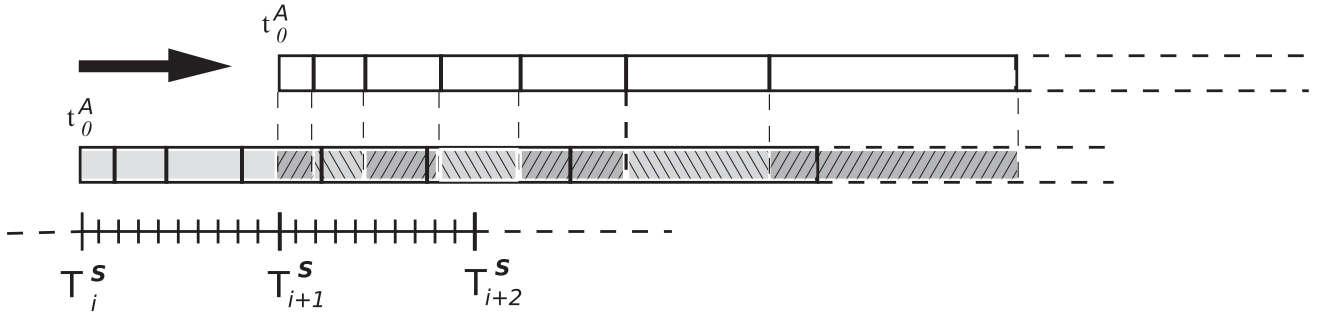


**Figure 3.** At the beginning of each snapshot, the RETURNEDMET array is pushed forward in time and re-aligned with the internal time evolution of the galaxy formation model. See text for details.

When the simulation starts, the time bins of the chemical evolution are set. We then build look-up tables that, for each time bin, contain the amount of every tracked chemical element produced by an SSP of 1 $M_{\odot}$. Look-up tables are calculated for all metallicity bins included in the yield tables adopted. In this way, we can significantly speed-up the calculations, that would otherwise require the estimation of double integrals (see equation (1)).

Looking at the example shown in Fig. 2, our method can be summarized as follows.

(i) When the galaxy is evolved from $T_i^S$ to $T_i^S + \delta\tau$, no star formation takes place. If the RETURNEDMET is empty (as e.g. at the very beginning of the simulation), nothing happens and the code just moves to the following time-step. Otherwise, the code reads from the array RETURNEDMET the amount of metals that needs to be re-incorporated (these metals were ejected by previous generations of stars) and proceeds to the next time-step.

(ii) During the second time-step, a star formation episode takes place. This is treated as an SSP, and the amounts of metals, energy and gas returned at any time in the future are calculated and stored in the RETURNEDMET array. The results of the calculation for the *i*th element and for the *j*th bin of the array, can be written as

$$\mathrm{OUT}_i^j = \int_{T_j^A}^{T_{j+1}^A} \mathrm{CHEMICAL\ EVOLUTION}_i(t, Z)\,\mathrm{d}t, \qquad (6)$$

where $T_0^A$, $T_1^A$, ..., $T_{n_{\mathrm{bins}}-1}^A$ are the times corresponding to the beginning of each bin in the RETURNEDMET array, and CHEMICAL EVOLUTION includes all the ingredients described above. The subscript $i$ runs from 1 to $n_{\mathrm{met}} + 2$ and refers to a heavy element (if $1 \le i \le n_{\mathrm{met}}$), the amount of H + He (if $i = n_{\mathrm{met}} + 1$), or the energy released by Sne (if $i = n_{\mathrm{met}} + 2$). In our specific model, the evolution depends only on time and metallicity (of the interstellar medium), but more generally it might depend on other physical properties of the interstellar medium, on the adopted initial mass function, etc. These additional ingredients could be easily included in the chemical evolution scheme implemented.

(iii) In addition to re-incorporating the metals ejected by previous generations of stars, the code also adds now into the future bins the elements produced by the new stars being formed. During the evolution between the two snapshots, the array RETURNEDMET is not pushed forward: the grey array shown in Fig. 2 is just a 'virtual' array used to distribute the metals in the appropriate time bin in the future.

(iv) Only when the code reaches the first time-step of the following snapshot, the array RETURNEDMET is moved forward in time and re-aligned with the internal time evolution of the galaxy formation model, as illustrated in Fig. 3. The reason for this is practical (to save memory), and is explained in detail in Appendix A.

In practice, our galaxy formation model uses integration time-steps that might not be negligible with respect to the relevant time-scales of the chemical evolution. In particular, this applies to elements produced after short delay times, and at earlier cosmic times, when the time spacing between subsequent snapshots is larger. Therefore, equation (6) should ideally be convolved with a non-delta-like star formation rate $\Psi$. For simplicity, we consider all the star formation events as impulsive in this work.

## 4 INFLUENCE OF CHEMICAL MODEL INGREDIENTS

As explained in the previous section, different approximations are made to include a detailed chemical enrichment treatment in our galaxy formation model, and different choices are possible for the model ingredients. In this section, we discuss the effects of using different (i) DTDs, (ii) yields, and (iii) number of time-bins for the chemical evolution. For this analysis, we will use the run Aq-A-3 but, as we show below, our physical model converges over the range of resolution sampled by the simulations considered in this study.

As mentioned earlier, we have fixed the value of the parameter $A$ so as to best reproduce the [Fe/H] and [O/Fe] distributions of disc stars for the model Milky Way (in the run Aq-A-3). A value of $A = 0.0014$ was chosen for all DTDs adopted in this study. We note that this value is in good agreement with those adopted in Matteucci et al. (2009) and Yates et al. (2013) (this latter study uses a different definition for the parameter $A$ – once this is accounted for, our preferred values are consistent). A single value for $A$ was also found to be suitable for different DTDs in the studies mentioned above.

### 4.1 DTDs

Fig. 4 shows the [Fe/H] (left-hand panels) and [O/Fe] (right-hand panels) distributions[3] for the stars in the model stellar disc of the simulation Aq-A-3, for different assumptions about the DTD. Black and grey histograms show observational measurements, while the coloured lines of different style show model results (the colour and style coding is the same as in Fig. 1). The model [Fe/H] distributions in the left-hand panels are compared with observational data

[3] To build these distributions, we attach to each model galaxy a 20 × 20 matrix that contains the information on the elemental abundances, and is updated each time an episode of star formation occurs.

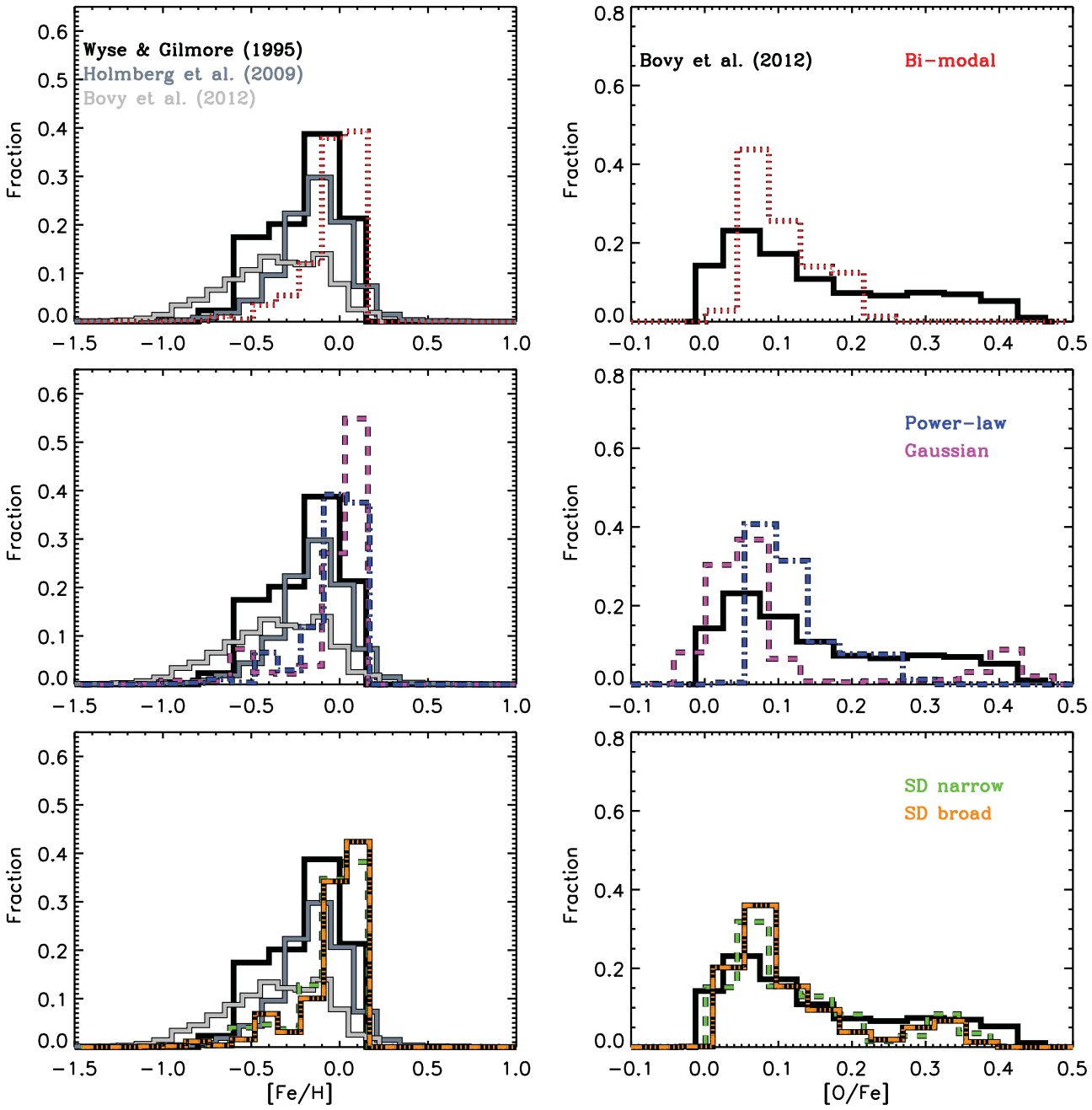


**Figure 4.** [Fe/H] (left-hand panels) and [O/Fe] (right-hand panels) distributions for the stars in the stellar disc of the run Aq-A-3 (the lowest resolution run used in this study), and different assumptions about the DTD (lines of different style and colour). Black and grey histograms show observational measurements by Wyse & Gilmore (1995), Holmberg, Nordström & Andersen (2009), and Bovy et al. (2012).

by Wyse & Gilmore (1995), Holmberg et al. (2009), and Bovy et al. (2012). The sample of Wyse & Gilmore (1995) represents a volume limited sample of long-lived thin disc G stars, while that of Holmberg et al. (2009) is based on the Geneva–Copenhagen Survey of the Solar Neighbourhood, a large (∼16 000) number of F and G dwarfs with improved astrometric distances from *Hipparcos* parallaxes. In both studies, metallicities were derived using a photometric calibration based on a relationship between [Fe/H] and Strömgren colours (e.g. Schuster & Nissen 1989). Finally, the sample defined in Bovy et al. (2012) is based on ∼300 G dwarfs from the Sloan Extension for Galactic Understanding and Exploration (SEGUE) survey. It should be noted that the SEGUE survey covers a wider range of galactic radii and significantly higher galactic scale heights with respect to the other two samples, that are limited to the solar neighbourhood. This likely explains the larger number of low-[Fe/H] stars in the Bovy et al. sample. For this sample, the quoted typical uncertainties are ∼0.2 dex for the spectroscopic values of [Fe/H], and ∼0.1 dex for [$\alpha$/Fe].

For all DTDs used in this study, the peaks of the predicted [Fe/H] distributions are approximately at the right location (shifted to slightly higher metallicities with respect to the observational measurements considered here). The predicted distributions are slightly narrower than the observed ones, and there is a lack of low-metallicity stars with respect to the sample by Wyse & Gilmore

(1995) and Bovy et al. (2012). One might expect that the distribution of the entire disc (that is what we predict) is broader than that of the solar neighbourhood (that is observed). On the other hand, one should consider that our model distributions are not convolved with the typical observational uncertainties (0.1–0.2 dex, or larger in case of estimates based on colours), which would tend to broaden them. In the right-hand panels of Fig. 4, we compare the observational [$\alpha$/Fe] distribution by Bovy et al. (2012) with the model predicted [O/Fe] distributions (O is the most abundant $\alpha$-element). In this case, model predictions vary significantly when changing the adopted DTD. The models that use the bi-modal and power-law DTDs (red dotted and blue dot–dashed histograms, corresponding to the red dotted and blue dot–dashed lines in Fig. 1) provide narrow distributions peaked around [O/Fe] $\sim$ 0.12. In contrast, when adopting a Gaussian DTD (magenta dashed) or a DTD corresponding to the single degenerate scenario (green long-dashed and orange triple dot–dashed), the predicted [O/Fe] distributions are broader, with a peak at low-[O/Fe] values close to that observed, and a more extended tail towards higher [O/Fe] values. Our results are consistent with those found by Yates et al. (2013) who included in their analysis three of the DTDs used here (the bi-modal, power law, and Gaussian). As they noted, the lack of any prompt component is in contradiction with recent observations (e.g. Maoz et al. 2012). In the following, we will adopt as our reference model the one constructed using the narrower single degenerate DTD shown in Fig. 1 (green long-dashed line). This provides the best agreement with observational measurements for both distributions shown in Fig. 4.

The differences between the distributions shown in the right-hand panels of Fig. 4 can be understood by analysing the evolution of the normalized number of SnIa events and of the effective [O/Fe] yield for an SSP of fixed metallicity. These are shown in Fig. 5 for different DTDs, using the same colour and style coding as in Figs 1 and 4. The abundance distribution results from the convolution of the galaxy's star formation history with the chemical evolution history, so that a detailed explanation of the predicted [O/Fe] distribution is not trivial. However, here we are interested in clarifying qualitatively the origin of the diverse distributions in the right-hand panels of Fig. 4, so we discuss the influence of the different DTDs adopted in this study neglecting the cumulative effect of subsequent stellar generations in order to highlight the underlying trend.

In the case of a bi-modal DTD (red dotted lines), the contribution from prompt SneIa is significant: the top panel shows that almost half of the SnIa events explode within $\sim$30 Myr. During this time interval, the effective [O/Fe] is high, because of the large oxygen contribution from SneII. Later on, the effective [O/Fe] yield decreases. It remains approximately constant for a relatively long time-scale, and then decreases slowly at late times. Therefore, one expects a large number of stars with intermediate/low [O/Fe] and a decreasing fraction at higher values, which is what we see in the top-right panel of Fig. 4. For a power-law DTD, the behaviour on time-scales $t \lesssim 4 \times 10^8$ yr is similar to that just described, while the evolution is significantly different for the other three DTDs considered, that have a significantly lower contribution from prompt SneIa. In particular, for a Gaussian DTD, all SnIa events explode after more than $\sim$1 Gyr, in a very short time interval. The effective [O/Fe] yield is therefore very high over this time-scale as significant amounts of oxygen are incorporated into the cold gas component before it starts being enriched with iron by SneIa. This leads to a prominent tail at high-[O/Fe] values, in addition to a large peak at low values of [O/Fe]. The behaviour of the two DTDs considered for the single degenerate model is intermediate, and the smooth evolution visible in Fig. 5 explains well the continuous distributions shown in Fig. 4.

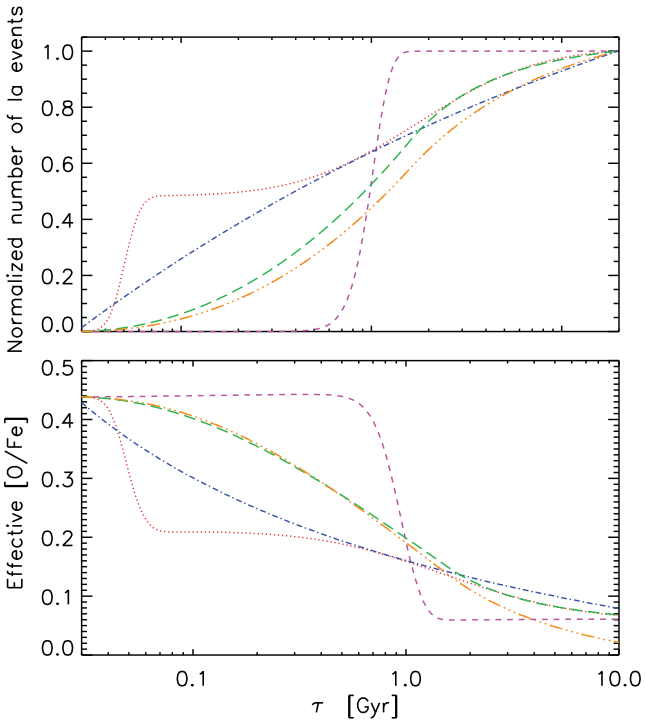


**Figure 5.** Normalized number of SnIa events (top panel) and effective [O/Fe] yield (bottom panel) for an SSP at fixed metallicity. Lines of different colour and style correspond to different DTDs (the same colour and style coding as in Figs 1 and 4 has been used: the blue dot–dashed line corresponds to the power-law DTD, the magenta dashed line to the narrow Gaussian DTD, the red dotted line to the bi-modal DTD, the green long dashed and orange triple dot–dashed lines to two different variations of the DTD corresponding to a single degenerate scenario.)

### 4.2 Yields and time-binning

Fig. 6 shows the same distributions as in Fig. 4, but this time the black solid histograms correspond to the reference model (the green long-dashed line in Fig. 1), while the coloured dashed and dotted histograms show the corresponding distributions obtained by either changing the yields (those from AGBs in the top panel and those from SneII in the middle panel) or by increasing the number of chemical time bins.

At metallicity around solar (the peak of the [Fe/H] distribution), the effective [O/Fe] yield by van den Hoek & Groenewegen (1997) is higher than that adopted in our reference model (that uses the yields by Karakas 2010). In addition, at variance with the yields by van den Hoek & Groenewegen (1997), those by Karakas (2010) account for some Fe contribution from AGBs. This explains why the [Fe/H] distribution shown by the red dashed histogram in the top left panel of Fig. 6 is shifted to slightly lower values, and there is a lower contribution of low-[O/Fe] stars with respect to the reference run. The differences between the black solid and blue dashed histograms in the middle panels of Fig. 6 is due to similar reasons: the yields by Woosley & Weaver (1995) give more iron than the corresponding yields adopted in our reference model (Chieffi & Limongi 2004), and a slightly lower [O/Fe] effective yield at solar metallicity.

The bottom panels of Fig. 6 show how the distributions considered vary increasing the number of chemical time-bins considered. The three distributions of [Fe/H] almost perfectly overlap (for clarity, we have introduced a horizontal shift in the figures), while larger variations are found for the distribution of [O/Fe]. These are due to small inaccuracies in the timings of re-incorporation of the metals

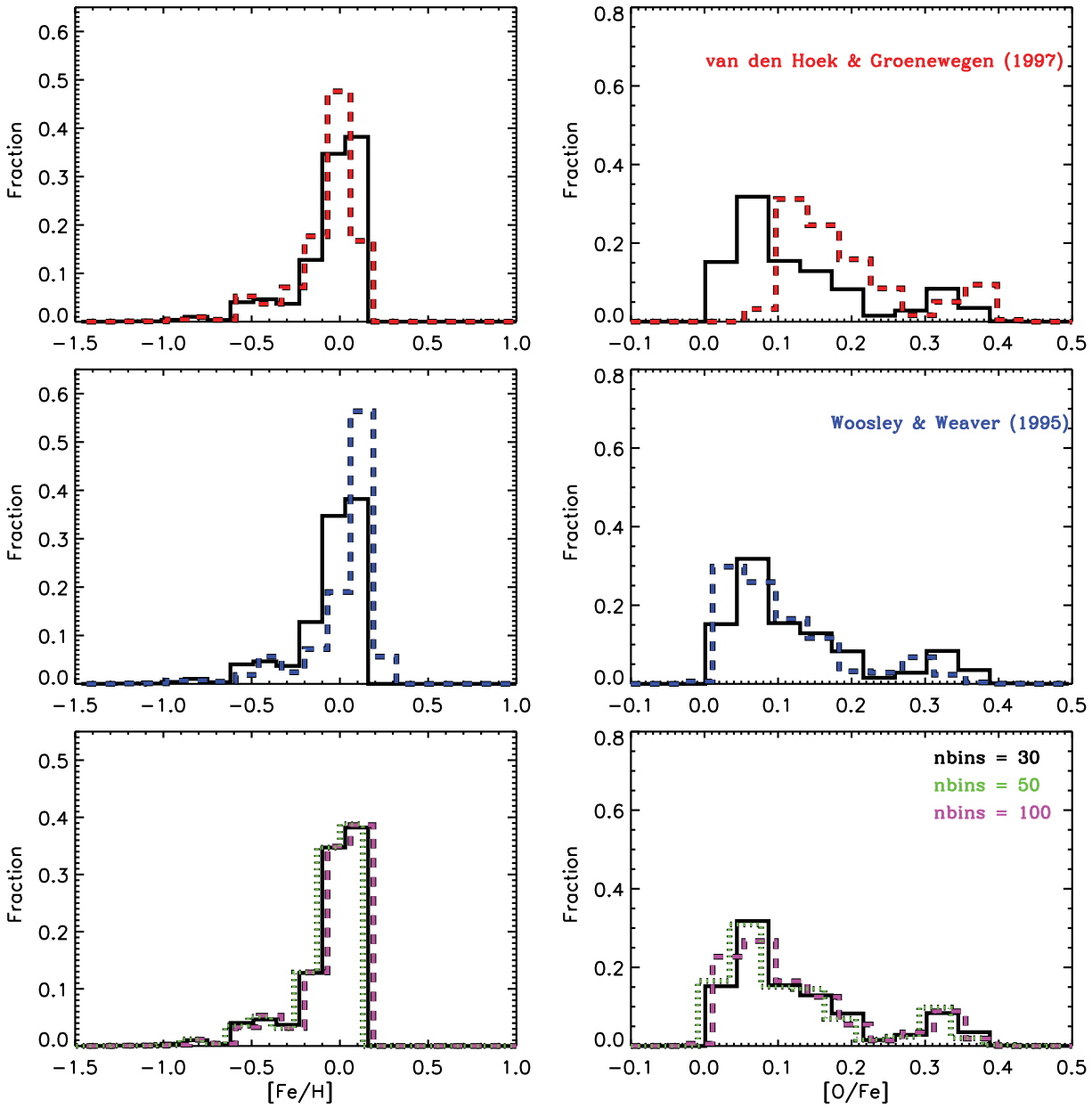


**Figure 6.** As in Fig. 4, but this time the black solid histograms refer to our reference model (see text for detail) and coloured dashed and dotted histograms correspond to different choices for the AGB yields (top panels), SnII yields (middle panels), and number of time bins for chemical evolution (bottom panels – gren dotted histograms show results for 50 timebins and dashed magenta histograms correspond to 100 timebins). Coloured histograms have been shifted horizontally by 0.03 (−0.03 for the green dotted line in the bottom panels) in the left-hand panel and 0.01 (−0.01 for the green dotted line in the bottom panels) in the right-hand panel for clarity.

because of the projection on a discrete array. The bottom panels of Fig. 6 show, however, that our results are stable against a significant increase in the number of chemical time bins adopted. We have also verified that results do not change when using alternative choices for the chemical bins (e.g. log-spaced bins, or fixed 'by hand').

## 5 EFFECT OF RELAXING THE INSTANTANEOUS RECYCLING APPROXIMATION

In the previous section, we have used the lowest resolution simulation considered in this study to investigate how our model results are influenced by several ingredients, and have used these results to identify our reference chemical model. We recall that this adopts the narrower single degenerate DTD shown in Fig. 1 (the green long-dashed line) and yields by Karakas (2010) for low- and intermediate-mass stars, Thielemann et al. (2003) for SneIa; and Chieffi & Limongi (2004) for SneII. As for our galaxy formation model, the parameters were kept fixed to those adopted in De Lucia & Helmi (2008) and Li et al. (2010). We will now discuss in more detail what are the predictions of our updated chemical model for the global properties of Milky Way galaxies, in the higher resolution runs used in our study.

Fig. 7 shows different physical properties of our model Milky Way galaxies, for all seven runs considered. Open circles show the results from the reference model using the IRA while filled

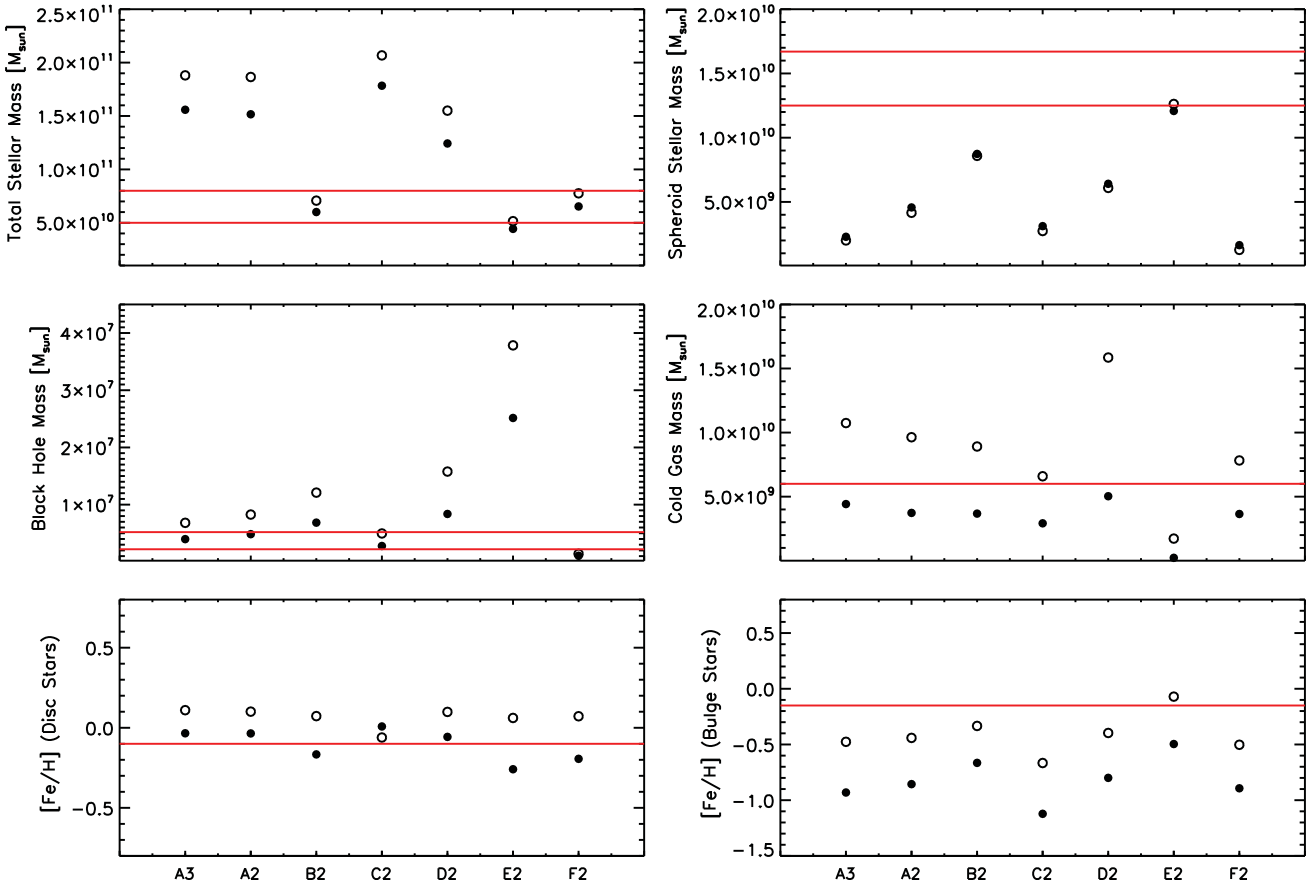


**Figure 7.** Physical properties of our model Milky Way galaxies, for the different simulations used in this study. Open circles show results from the model based on the IRA, while filled symbols show the corresponding results based on the updated chemical model presented in this paper. Red horizontal lines in each panel indicate observational estimates.

symbols show the corresponding results based on the updated chemical model presented in this paper. Red horizontal lines in each panel indicate the observational range/estimates.

The estimated stellar mass of our Milky Way is $\sim 5$–$8 \times 10^{10}$ $M_\odot$ (e.g. Flynn et al. 2006). The top-left panel of Fig. 7 shows that only three of the simulations used in this study predict stellar masses within this range (these are Aq-B-2, Aq-E-2, and Aq-F-2). For all the other runs, the predicted stellar mass is larger than the observational estimate by a factor $\sim 2.5$. All runs predict a spheroidal stellar mass that is lower than the observational estimate ($\sim 25$ per cent of the disc stellar mass, Bissantz, Debattista & Gerhard 2004), except for the run Aq-E-2 (this confirms results found in De Lucia & Helmi 2008 based on lower resolution simulations). We recall that, as discussed in Section 2, our model does not include any prescription for bulge formation during disc instability events. This would be required for an appropriate comparison with the bulge of our Milky Way.

The middle-left panel of Fig. 7 shows that the predicted black hole mass is not far off the observational estimate (Schödel et al. 2002), but for the run Aq-E-2. This is a consequence of the fact that the galaxy formation model has been tuned to reproduce the locally observed relation between the mass of the black hole and the mass of the bulge, and that the black hole at the centre of our Galaxy is known to be offset with respect to such a relation. The amount of cold gas predicted by our model is slightly lower than estimated values (Blitz 1997, and references therein). Finally, the bottom panels of Fig. 7 show that the predicted average metallicities are not far from the observational estimate for the stellar disc but significantly lower than suggested by data for the bulge component (Freeman & Bland-Hawthorn 2002). We note that the [Fe/H] values plotted in these panels for the runs adopting an IRA have been obtained by scaling the total metallicities by the appropriate ratio computed using the corresponding run based on our updated chemical model. In the following section, we will analyse the metallicity distributions predicted for both stellar components in more detail, and compare them with observational estimates.

For all runs, our updated chemical model provides stellar masses that are lower than the corresponding values obtained using the same model parameters in a scheme that adopts the IRA. It is worth noting, however, that the predicted stellar mass varies significantly depending on the halo merger history. Also the black hole mass, the gas mass and the mean metallicity of both the disc and bulge stellar components are systematically lower in the updated chemical model, while the stellar masses of the spheroidal component are slightly larger in this model with respect to the corresponding values obtained by adopting the IRA. We will come back to the difference between the two schemes at the end of this section.

Fig. 8 shows the total star formation history of our model Milky Way galaxies (this has been obtained by summing, at each time, the star formation rates of all progenitors of the final Milky Way

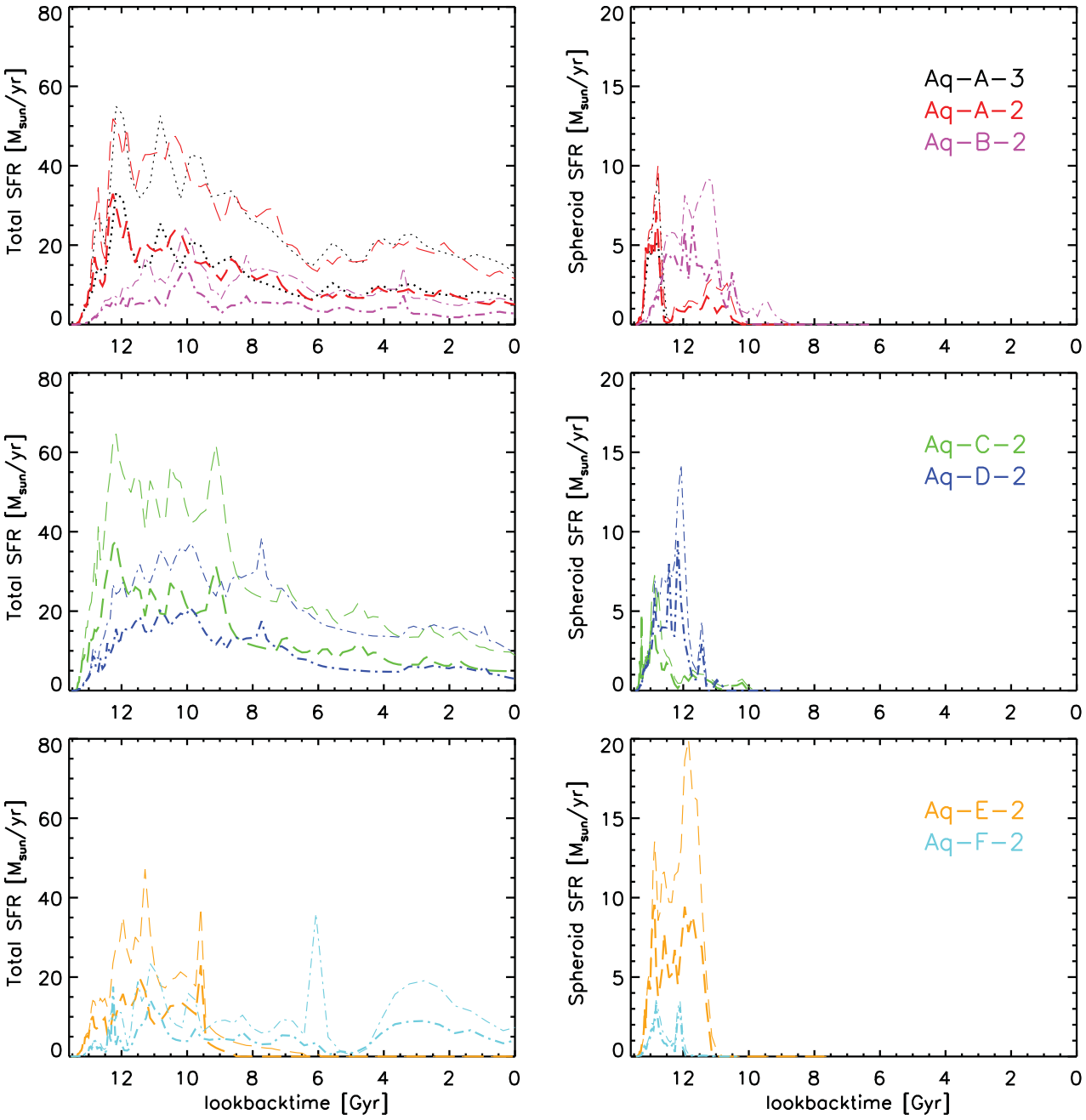


**Figure 8.** Star formation history of our model Milky Way galaxies, from the different simulations used in this study. The left-hand panels show the total star formation history, while the right-hand panels correspond to the star formation history of the spheroidal component. Thin lines show results from the model based on the IRA, while thick lines show the corresponding results based on the updated chemical model presented in this paper. Dotted lines are used for Aq-A-3, while for the level 2 simulations, dashed and dot–dashed lines are used for the first and second simulation indicated in the legend of each row.

galaxy, left-hand panels), and that of the stars in the spheroidal components (right-hand panels), for all seven runs used in this study. Results from the two resolution levels considered for run Aq-A show very good convergence (compare black dotted and red dashed lines in the top panels). For all runs considered in this study, the total star formation history is fairly extended, with present day values ranging between almost zero for Aq-E-2 and $\sim 6\,M_\odot\ yr^{-1}$ for Aq-A-2. With the exception of Aq-E-2, the present level of star formation activity is still somewhat higher than the $\sim 2\,M_\odot\ yr^{-1}$ estimated for the mean star formation rate in the Milky Way disc (Chomiuk & Povich 2011), but systematically lower than the corresponding values found in our previous model based on the IRA. All stars that currently reside in the spheroidal component of our model Milky Way galaxies formed more than ∼10 Gyr ago. The peak of the star formation is never higher than $\sim 10\,M_\odot\ yr^{-1}$, while the typical width ranges between 1 and 3 Gyr. As we will see in the next section, this has important consequences for the metallicity distribution of the spheroidal component. Generally, the star formation rates from our updated chemical model are systematically lower than those obtained from the corresponding runs assuming an IRA, at all times. For the spheroidal component, this systematic difference is lower, and negligible for the runs Aq-A-2, Aq-C-2, and Aq-F-2.

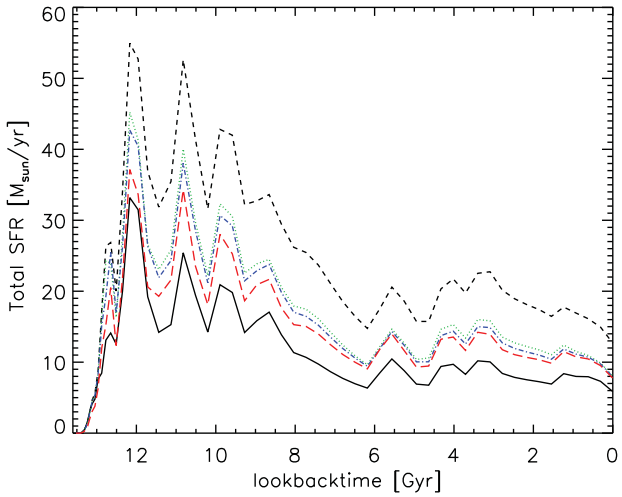


**Figure 9.** Star formation history for the model Milky Way galaxy in the run Aq-A-3. The solid black line shows the prediction from the reference model used in this study, while the black dashed line shows the corresponding prediction from a run that adopts an IRA. The coloured dotted, dot–dashed and long-dashed lines corresponds to variations of the latter run with varying parameters (see text for details).

Naively, the lower star formation rate in the updated chemical scheme can be attributed to the slower recycling of gas from massive stars with respect to a scheme adopting an IRA. To better understand the differences between the two schemes, and quantify them in terms of (i) amount of cold gas recycled from stars, (ii) chemical yields, and (iii) energy injected into the cold gas by Sn explosions, we have carried out several additional runs using Aq-A-3, and varying the relevant parameters in the run assuming an IRA. As explained in Section 2, this model assumes an instantaneous recycling fraction $R = 0.43$ (corresponding to the integral contribution of H+He from SneII, SneIa, and AGBs for the Chabrier IMF assumed in our study), a constant yield $Y = 0.03$, and a number of Sn events per unit stellar mass formed $\eta_{\rm SN} = 8 \times 10^{-3}$.

The amount $R$ of cold gas restored by Sn explosions has a major effect since it directly and promptly affects the reservoir of gas available for star formation. The effective yield $Y$ acts on the star formation through the dependence on the metallicity of the cooling function, so that the higher its value the shorter is the cooling time. Finally, the energy injected by Sn explosions delays or prevents star formation in the surrounding gas by reheating part of it.

In order to show the cumulative effect of these quantities, we changed them one at a time in the run adopting the IRA, so as to be consistent with the values used in the updated chemical model. In this case, the recycled fraction $R$ is consistent with that adopted in the run with instantaneous recycling, with a weak dependence on the adopted yields and the metallicity of the star. However, in the updated chemical scheme, this fraction of gas is ejected into the interstellar medium over about 10 Gyr, as discussed in previous sections. In order to mimic the effect of this dilution in the run based on the IRA, we set $R = 0.15$ that is the fraction of H+He restored by SneII only. As for the effective yield, our tables are consistent with the assumption $Y = 0.02$. Finally, we assume $\eta_{\rm SN} = 0.014$, that is the total number of both SnII ($\eta_{\rm SNII} = 0.012$) and SnIa ($\eta_{\rm SNIa} = 0.0018$) events per unit stellar mass formed.

Results of this analysis are shown in Fig. 9. The dashed and solid black lines show the two reference runs with an IRA and updated chemical model, respectively. The dotted green line in Fig. 9 corresponds to a run adopting the IRA but $R = 0.15$. In this run, the star formation rates are reduced with respect to the dashed black lines at all times, but are still significantly higher than those corresponding to our updated chemical model. The dot–dashed blue line shows the results obtained by further reducing the effective yield to $Y = 0.02$, that is closer to that adopted in our chemical model. Finally, the long-dashed red line corresponds to a run that adopts $R = 0.15$, $Y = 0.02$, and $\eta_{\rm SN} = 0.014$ that is the appropriate number based on our choice of IMF and model for SneIa. At early times (lookback time larger $\sim$11.5 Gyr), the star formation rates obtained for this last model are very close to those resulting from our updated chemical model. At late times, the results tend to diverge because of the contribution from late recycling of gas and metals, and its effects on the metallicity of the hot gas and gas cooling rates.

## 6 MILKY WAY DISC, SPHEROID AND SATELLITES

In the previous sections, we have analysed in detail the dependence of our results on various model ingredients, as well as the global properties and star formation histories of all runs used in our study. We now turn to the predicted metallicity distributions of the disc and spheroid components. The [Fe/H] distributions are shown in Fig. 10. Left-hand panels correspond to the model disc, while right-hand panels to the spheroid. Black and grey histograms show different observational measurements, and coloured dashed and dot–dashed lines show model predictions for the six level-2 resolution haloes considered in this study.

We remind that we have 'tuned' our model by considering primarily the [Fe/H] and [O/Fe] metallicity distributions of the disc component for the run Aq-A-3. The left-hand panels of Fig. 10 show that, for the same combination of model parameters and ingredients, similar [Fe/H] distributions are obtained for all six haloes considered. Considering the uncertainties in the observational data, all of them appear to be in reasonable agreement with measurements of our Milky Way disc stars. This is not surprising given the similar behaviour of star formation histories plotted in the left-hand panels of Fig. 8. Aq-A-2 and Aq-C-2 have very similar star formation histories, with a slightly more significant peak at early cosmic epochs for the run Aq-A-2. This explains why the red and green dashed histograms (in the top and middle panels) in the left-hand panels of Fig. 10 are very similar with a slightly larger fraction of high-[Fe/H] stars in the run Aq-C-2. For the run Aq-D-2, the star formation history is broader, and so is the corresponding [Fe/H] distribution. Aq-B-2 is again very similar to Aq-A-2 but the overall level of star formation rate is lower, which explains why the peak of the [Fe/H] distribution is shifted to slightly lower values of [Fe/H] with respect to that of Aq-A-2. Finally, for the runs Aq-E-2 and Aq-F-2, the star formation rates are always lower than $\sim 20\,{\rm M}_{\odot}\,{\rm yr}^{-1}$. The star formation rate drops to virtually zero after the first $\sim$4 Gyr for the run Aq-E-2, and shows a late 'bump' of star formation for the run Aq-F-2. As a consequence, the [Fe/H] distributions are very narrow, with a somewhat larger contribution from stars with high [Fe/H] in the run Aq-F-2.

For all six level-2 haloes, the star formation history of the spheroid component is relatively narrow and peaked at high redshift. In addition, the actual values of the star formation rate are relatively modest. This translates into metallicity distributions that are offset low with respect to the observational estimates. The largest fraction of high-[Fe/H] stars is obtained for the run Aq-E-2 whose spheroid component exhibits a relatively broad (compared to the other runs)

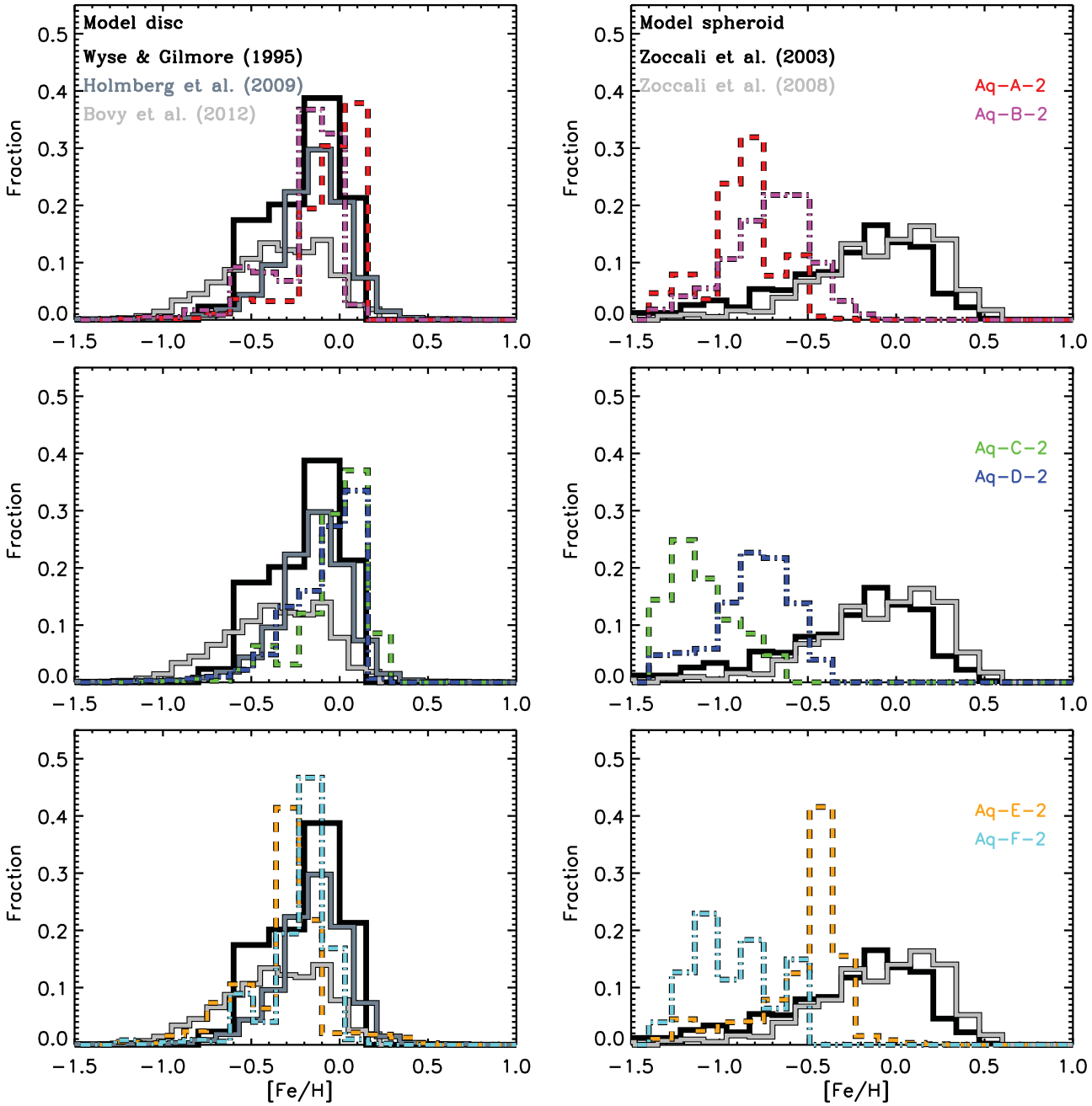


**Figure 10.** [Fe/H] distributions of the stars in the stellar disc (left-hand panels) and spheroid (right-hand panel) for all the simulations used in this study (dashed and dot–dashed histograms corresponding to the first and second simulation indicated in the legend for each row, respectively), compared with different observational determinations (black and grey histograms).

star formation history at levels that are the highest compared to those of the other runs. For this run, however, the peak of the [Fe/H] metallicity distribution is also lower than the observed location by about 0.5 dex. As noted in the previous section, our model neglects any contribution to bulge formation through disc instabilities. If these occur late during the evolution of the Milky Way, they could contribute to populating the high-[Fe/H] tail of the distributions in our model. Given the uncertainties in modelling dynamical disc instabilities, and the fine-tuning that appears to be required to reproduce the observational measurements, we prefer not to investigate this issue further in this work.

Do any of the runs considered in this study give a model galaxy that is in reasonable agreement with both the global properties and the metallicity distributions of our Milky Way? Forgetting about the too low metallicity of the spheroid component, the run that provides the best match is probably Aq-B-2. For this run, the predicted stellar mass of the model Milky Way galaxy is $\sim 6 \times 10^{10}\,\mathrm{M}_{\odot}$, in very good agreement with the estimated stellar mass for our Galaxy. The mass of the spheroidal component (we recall that our runs do not include any disc instability channel) is $\sim 8.7 \times 10^{9}\,\mathrm{M}_{\odot}$, slightly below the observationally estimated value. The current level of star formation rate is $\sim 2.8\,\mathrm{M}_{\odot}\,\mathrm{yr}^{-1}$, and the present value of the SnIa

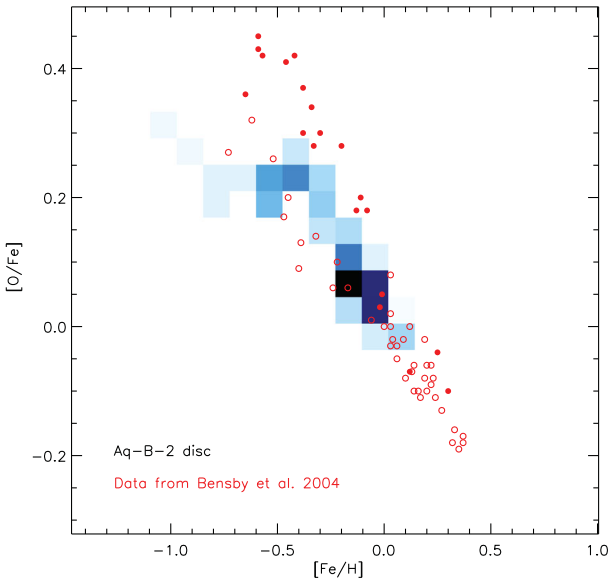


**Figure 11.** [O/Fe] versus [Fe/H] distribution for the stars in the stellar disc of the simulation Aq-B-2. Red circles show observational measurements from Bensby, Feltzing & Lundström (2004), with filled and open symbols corresponding to thick and thin disc stars, respectively.

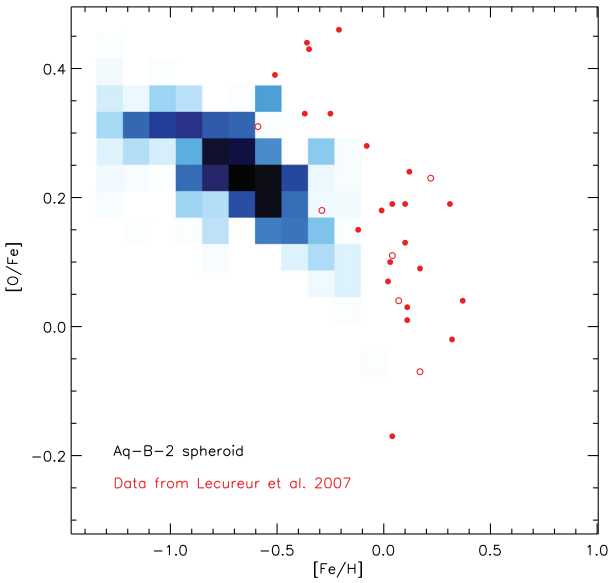


**Figure 12.** As for Fig. 11 but for the stars in the spheroid of the simulation Aq-B-2. Red circles show observational measurements from Lecureur et al. (2007), with open symbols corresponding to uncertain O abundances.

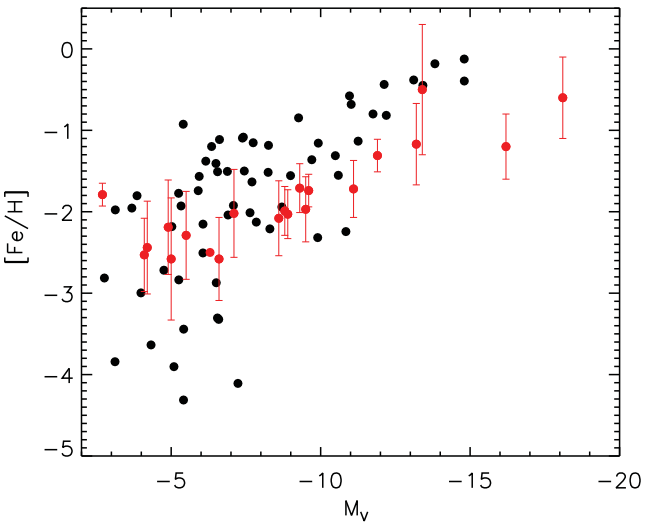


**Figure 13.** Metallicity–luminosity relation for the satellites. Filled black symbols show model predictions for all satellite galaxies in the Aq-B-2 run within 280 kpc from the central model Milky Way. Red filled symbols with error bars show observational measurements for both the 'classical' and ultrafaint satellites. Model data points have been shifted by −0.23 dex (see text for details).

rate is 0.58 events/century (two or three times larger than the observational estimate of ∼0.2–0.3 events/century – see e.g. Cappellaro, Evans & Turatto 1999 and Li et al. 2011). The recent work by Starkenburg et al. (2013), based on our reference model with the IRA, reached the same conclusion as for the galaxy that most closely resembles the Milky Way. Interestingly, they showed that the same run has also a satellite luminosity function in quite good agreement with observational measurements but does not contain satellites as bright as the Small or Large Magellanic Clouds. As they note (see their section 6.2), with the adopted star formation and feedback prescriptions, our best Milky Way galaxy corresponds to a dark matter halo with mass $8 \times 10^{11}$ $M_{\odot}$, that is on the low end of observational estimates (Smith et al. 2007; Xue et al. 2008; Li & White 2008). In addition, over the mass range probed by the Aquarius haloes, the relation between dark matter halo mass and stellar mass for central galaxies is offset with respect to that derived using abundance matching methods by e.g. Guo et al. (2010) that is reproduced (by construction) in the model by Guo et al. (2011).

Figs 11 and 12 show the [O/Fe] versus [Fe/H] metallicity distributions for both the stellar disc and the spheroid component of the model Milky Way galaxy in the run Aq-B-2. The 2D distributions from the other runs are actually very similar. As discussed above, the [Fe/H] metallicity distribution is in quite good agreement with observational data of the thin disc (in part by construction). In contrast, stars in the spheroid are significantly metal poorer than observed. Finally, stars in both components cover approximately the same range of [O/Fe] abundances as the data.

Fig. 13 shows the metallicity–luminosity relation for all the satellite galaxies of the Aq-B-2 run within 280 kpc from the central galaxy. Filled black circles show model predictions while red filled symbols with error bars show observational measurements for both the 'classical' and ultrafaint satellites (we have used the compilation of the literature data by Li et al. 2010). As noted by Starkenburg et al. (2013), our metallicities are mass-weighted while the observational measurements are mean [Fe/H], that they find to be on average 0.23 dex lower than the logarithm of the average over the ratio of Fe to H. Therefore, we have shifted by −0.23 dex the model data points in Fig. 13 (this shift, however, is not significant on the scale shown).

As mentioned above, the run Aq-B-2 does not contain satellites as bright as the two brightest members of the Local Group (the LMC and SMC). Overall, the model metallicity–luminosity relation is in relatively good agreement with data, although the model relation appears to be offset slightly higher and to have a somewhat steeper slope than observed. Nevertheless, the level of agreement with data shown in Fig. 13 is remarkable, given that these data were not considered when tuning our chemical model. It remains to be seen

if the same model is able to reproduce also the vast amount of chemical data available for the more general galaxy population, both in the local Universe and at higher redshift. We will address this issue in future work.

## 7 DISCUSSION AND CONCLUSIONS

We have presented a new method to account for relaxing the IRA and trace individual elemental abundances within a semi-analytic model of galaxy formation and evolution. The model we use in this paper is based on the model described in detail in De Lucia & Blaizot (2007) but has been refined to follow more accurately processes on the scale of the Milky Way's satellites (for details, we refer to De Lucia & Helmi 2008, Li et al. 2010, and Starkenburg et al. 2013). We take advantage of the simulations carried out within the Aquarius Project (Springel et al. 2008): a sample of six haloes of roughly Milky Way mass and with no massive close neighbour at $z = 0$, all simulated at the same level of resolution (corresponding to a particle mass between $m_{\rm p} = 6.45 \times 10^3$ and $m_{\rm p} = 1.40 \times 10^4\,{\rm M}_{\odot}$). To analyse the convergence of the physical model and study the influence of different model ingredients, we also take advantage of one lower resolution run, with a particle mass of $m_{\rm p} = 4.91 \times 10^4\,{\rm M}_{\odot}$.

All previously published models that implement a detailed description of chemical evolution (Nagashima et al. 2005; Arrigoni et al. 2010; Benson 2012; Yates et al. 2013) adopt a similar method to account for the finite lifetime of stars: the past star formation history is re-binned and stored in memory. This information is then used to compute the metal restitution rates at any time during model integration. Since the calculation requires an averaging of individual star formation events, it becomes increasingly inaccurate as the time elapsed between star formation events increases, i.e. for long-living stars whose accounting represents the main reason to implement an algorithm that relaxes the IRA. We have developed a new method that instead computes the metal ejection rates every time new stars are formed, and stores this information in the future. While a binning is also necessary (to avoid memory overheads), the method allows an accurate accounting of the timings and properties of individual star formation events.

The model extension discussed above requires the introduction of new model ingredients, and a number of assumptions. We have analysed, in particular, the influence of (i) different DTDs for SneIa; (ii) different yields; (iii) number of chemical time bins adopted. These have an important influence on the predicted [O/Fe] distributions for stars in the disc of the model Milky Way galaxies. In particular, DTDs with a less significant prompt component predict broader distributions with a more extended tail towards high-[O/Fe] values. This is because significant amounts of oxygen (produced by SneII) can be incorporated into the cold gas component before it starts being enriched with iron by SneIa. Our reference chemical model assumes a DTD based on the single degenerate model described by Matteucci & Recchi (2001) and corresponds to a fraction of prompt SneIa of about 5 per cent (if 'prompt' is defined as exploding within $10^8$ yr from the star formation episode, the fraction increases to about 23 per cent when considering all SnIa events within $4 \times 10^8$ yr). Our findings are consistent with (but stronger than) results from Yates et al. (2013) who require $\lesssim$50 per cent of the SneIa within $4 \times 10^8$ yr. Different sets of yields for SneII and AGBs can affect significantly the metallicity distributions of disc stars, depending on the relative contribution of iron and oxygen. We have shown that our results are stable against a significant increase in the number of adopted chemical time bins, as well as against the choice of time-bins. In particular, in our reference model, bins are chosen in such a way that each contains a constant number of events. Results do not change if bins are log-spaced in time, or simply fixed 'by hand'.

There are degeneracies in the chemical model ingredients: e.g. a different DTD than the one adopted in our reference model, combined with a different set of yields might provide very similar results in terms of the metallicity distribution. However, once a reference model has been chosen, the results listed below remain valid. In particular, tuning the model considering mainly the [Fe/H] and [O/Fe] metallicity distributions of the disc component in the lowest resolution run, we find that:

(i) our updated chemical model results in a systematically lower star formation history with respect to runs adopting the same physical model but based on an IRA. This is a consequence of a lower effective yield and number of Sn events in our updated chemical model, as well as of the slower recycling of gas, metals and energy from massive stars. The latter has important consequences on the metallicity of the hot gas component and gas cooling rates.

(ii) For all runs, the [Fe/H] metallicity distributions of the disc stars are in reasonable agreement with observational measurements. The star formation history of the spheroid component is relatively narrow and peaked at high redshift. This results into a metallicity distribution that is offset low with respect to observational data. Our runs do not include a disc instability channel for bulge formation. These events could help to populate the high-[Fe/H] tail of the metallicity distributions, but a certain level of fine-tuning appears to be required in order to reproduce the observational data.

(iii) The six haloes used in this study provide a range of predicted properties for the model Milky Way. Among these, the one that most resembles our Galaxy is Aq-B-2. For this particular run, we have shown that not only the global properties of the Milky Way are well reproduced, but also the observed relation between the average metallicity of the satellite galaxies and their luminosity (albeit with a slightly steeper slope).

In this paper, we have only applied our updated chemical scheme to Milky Way-like haloes and analysed the dependence on different model ingredients and basic predictions. In future work, we plan to extend the analysis to other components of the Milky Way (in particular the stellar halo), as well as to different cosmic epochs and galaxy types. By analysing the metallicity distributions in different baryonic components, and the dependence on the feedback and recycling scheme, our model should be able to provide important constraints on these physical processes.

## ACKNOWLEDGEMENTS

GDL acknowledges financial support from the European Research Council under the European Community's Seventh Framework Programme (FP7/2007-2013)/ERC grant agreement no. 202781. We acknowledge fruitful and stimulating discussions with Francesca Matteucci, Simone Recchi, and Donatella Romano. We thank J. Bovy for providing us with his data in electronic format, and S. Recchi, D. Romano, R. Yates, and E. Starkenburg for constructive comments on a preliminary version of this manuscript. We are indebted to Volker Springel for making the merger trees from the Aquarius haloes available to us. We thank the referee, Christopher Few, for his constructive and positive feedback.

## REFERENCES


Arrigoni M., Trager S. C., Somerville R. S., Gibson B. K., 2010, MNRAS, 402, 173
Battaglia G. et al., 2005, MNRAS, 364, 433
Baugh C. M., 2006, Rep. Prog. Phys., 69, 3101
Bensby T., Feltzing S., Lundström I., 2004, A&A, 415, 155
Benson A. J., 2012, New. Astron., 17, 175
Bissantz N., Debattista V. P., Gerhard O., 2004, ApJ, 601, L155
Blitz L., 1997, in Latter W. B., Radford S. J. E., Jewell P. R., Mangum J. G., Bally J., eds, Proc. IAU Symp. Vol. 170, CO in the Milky Way. Kluwer, Dordrecht, p. 11
Bonaparte I., Matteucci F., Recchi S., Spitoni E., Pipino A., Grieco V., 2013, MNRAS, 435, 2460
Bovy J., Rix H.-W., Liu C., Hogg D. W., Beers T. C., Lee Y. S., 2012, ApJ, 753, 148
Boylan-Kolchin M., Springel V., White S. D. M., Jenkins A., Lemson G., 2009, MNRAS, 398, 1150
Boylan-Kolchin M., Springel V., White S. D. M., Jenkins A., 2010, MNRAS, 406, 896
Cappellaro E., Evans R., Turatto M., 1999, A&A, 351, 459
Chabrier G., 2003, PASP, 115, 763
Chieffi A., Limongi M., 2004, ApJ, 608, 405
Chomiuk L., Povich M. S., 2011, AJ, 142, 197
Cooper A. P. et al., 2010, MNRAS, 406, 744
Cora S. A., 2006, MNRAS, 368, 1540
De Lucia G., Blaizot J., 2007, MNRAS, 375, 2
De Lucia G., Helmi A., 2008, MNRAS, 391, 14
De Lucia G., Kauffmann G., White S. D. M., 2004, MNRAS, 349, 1101
De Lucia G., Fontanot F., Wilman D., Monaco P., 2011, MNRAS, 414, 1439
Dwek E. et al., 1995, ApJ, 445, 716
Few C. G., Courty S., Gibson B. K., Kawata D., Calura F., Teyssier R., 2012, MNRAS, 424, L11
Flynn C., Holmberg J., Portinari L., Fuchs B., Jahreiß H., 2006, MNRAS, 372, 1149
Freeman K., Bland-Hawthorn J., 2002, ARA&A, 40, 487
Graves G. J., Faber S. M., Schiavon R. P., 2009, ApJ, 698, 1590
Greggio L., 2005, A&A, 441, 1055
Guo Q., White S., Li C., Boylan-Kolchin M., 2010, MNRAS, 404, 1111
Guo Q. et al., 2011, MNRAS, 413, 101
Guo Q., White S., Angulo R. E., Henriques B., Lemson G., Boylan-Kolchin M., Thomas P., Short C., 2013, MNRAS, 428, 1351
Hillebrandt W., Kromer M., Röpke F. K., Ruiter A. J., 2013, Frontiers Phys., 8, 116
Holmberg J., Nordström B., Andersen J., 2009, A&A, 501, 941
Iben I., Jr, Tutukov A. V., 1984, ApJ, 284, 719
Karakas A. I., 2010, MNRAS, 403, 1413
Lecureur A., Hill V., Zoccali M., Barbuy B., Gómez A., Minniti D., Ortolani S., Renzini A., 2007, A&A, 465, 799
Li Y.-S., White S. D. M., 2008, MNRAS, 384, 1459
Li Y.-S., De Lucia G., Helmi A., 2010, MNRAS, 401, 2036
Li W., Chornock R., Leaman J., Filippenko A. V., Poznanski D., Wang X., Ganeshalingam M., Mannucci F., 2011, MNRAS, 412, 1473
McWilliam A., 1997, ARA&A, 35, 503
Maeder A., Meynet G., 1989, A&A, 210, 155
Mannucci F., Della Valle M., Panagia N., 2006, MNRAS, 370, 773
Maoz D., Mannucci F., Brandt T. D., 2012, MNRAS, 426, 3282
Matteucci F., 1994, A&A, 288, 57
Matteucci F., 2008, in Grebel E., Moore B., eds, Proc. 37th Saas-Fee Advanced Course of the Swiss Society for Astrophysics and Astronomy, The Origin of the Galaxy and the Local Group. Springer-Verlag, Berlin, p. 145
Matteucci F., Recchi S., 2001, ApJ, 558, 351
Matteucci F., Panagia N., Pipino A., Mannucci F., Recchi S., Della Valle M., 2006, MNRAS, 372, 265
Matteucci F., Spitoni E., Recchi S., Valiante R., 2009, A&A, 501, 531
Nagashima M., Lacey C. G., Baugh C. M., Frenk C. S., Cole S., 2005, MNRAS, 358, 1247
Oppenheimer B. D., Davé R., 2006, MNRAS, 373, 1265
Padovani P., Matteucci F., 1993, ApJ, 416, 26
Pignatari M. et al., 2013, preprint (arXiv:1307.6961)
Pipino A., Devriendt J. E. G., Thomas D., Silk J., Kaviraj S., 2009, A&A, 505, 1075
Portinari L., Chiosi C., Bressan A., 1998, A&A, 334, 505
Romano D., Chiappini C., Matteucci F., Tosi M., 2005, A&A, 430, 491
Romano D., Karakas A. I., Tosi M., Matteucci F., 2010, A&A, 522, A32
Ruiz-Lapuente P., Canal R., 1998, ApJ, 497, L57
Scannapieco C., Tissera P. B., White S. D. M., Springel V., 2005, MNRAS, 364, 552
Schödel R. et al., 2002, Nature, 419, 694
Schuster W. J., Nissen P. E., 1989, A&A, 221, 65
Smith M. C. et al., 2007, MNRAS, 379, 755
Springel V., White S. D. M., Tormen G., Kauffmann G., 2001, MNRAS, 328, 726
Springel V. et al., 2005, Nature, 435, 629
Springel V. et al., 2008, MNRAS, 391, 1685
Stanek K. Z., Mateo M., Udalski A., Szymanski M., Kaluzny J., Kubiak M., 1994, ApJ, 429, L73
Starkenburg E. et al., 2013, MNRAS, 429, 725
Strolger L.-G. et al., 2004, ApJ, 613, 200
Thielemann F.-K. et al., 2003, in Hillebrandt W., Leibundgut B., eds, From Twilight to Highlight: The Physics of Supernovae Supernova Nucleosynthesis and Galactic Evolution. Springer-Verlag, Berlin, p. 331
Thomas D., Greggio L., Bender R., 1999, MNRAS, 302, 537
Tinsley B. M., 1979, ApJ, 229, 1046
Tinsley B. M., 1980, Fundam. Cosm. Phys., 5, 287
Tornatore L., Borgani S., Matteucci F., Recchi S., Tozzi P., 2004, MNRAS, 349, L19
Tornatore L., Borgani S., Viel M., Springel V., 2010, MNRAS, 402, 1911
van den Hoek L. B., Groenewegen M. A. T., 1997, A&AS, 123, 305
Vásquez S. et al., 2013, A&A, 555, A91
Wang B., Han Z., 2012, New Astron. Rev., 56, 122
Wang J., De Lucia G., Kitzbichler M. G., White S. D. M., 2008, MNRAS, 384, 1301
Webbink R. F., 1984, ApJ, 277, 355
Whelan J., Iben I., Jr, 1973, ApJ, 186, 1007
Wiersma R. P. C., Schaye J., Theuns T., Dalla Vecchia C., Tornatore L., 2009, MNRAS, 399, 574
Woosley S. E., Weaver T. A., 1995, ApJS, 101, 181
Worthey G., Faber S. M., Gonzalez J. J., 1992, ApJ, 398, 69
Wyse R. F. G., Gilmore G., 1995, AJ, 110, 2771
Xue X. X. et al., 2008, ApJ, 684, 1143
Yates R. M., Henriques B., Thomas P. A., Kauffmann G., Johansson J., White S. D. M., 2013, MNRAS, 435, 3500


## APPENDIX A: SLIDING AND RE-BINNING OF THE METAL ARRAY

In general, the size of the sub-step $\delta\tau$ and of the RETURNEDMET timebins are independent from each other, and generally treated as free parameters that can be modified according to memory and computational time constraints. In addition, $\delta\tau$ can change from one snapshot to another if the snapshot times are not equally spaced. Therefore, in general, $\delta\tau$ could correspond to 0 or several entries in RETURNEDMET or will fall within one of its entries.

When the code evolves the galaxy $G$ from a sub-step to the next one, a fraction $f = \delta\tau/\Delta T_0^A$ of the relevant entry of the array RETURNEDMET is re-incorporated (and subtracted from RETURNEDMET). Then RETURNEDMET should be shifted forward in time by $\delta\tau$, and all its entries should be re-binned so that a fraction $f_j = \delta\tau/\Delta T_j^A$ of the $j$th entry flows in the previous entry RETURNEDMET $[j-1]$. It is easy to compute that the first entry should contain

$$Z_0 \times (1 - f_0) + Z_1 \times f_1$$

and that, after another $\delta\tau$, it should contain

$$Z_0 \times (1 - 2 \times f_0) + Z_1 \times f_1 \times (f_0) + Z_1 \times f_1.$$

Therefore, a correct re-binning requires a separate storage of the $Z_j$ elements at each sub-step, which again leads to a dramatic memory overhead. In addition, if new stars are formed, new metals are produced and should be added to the various entries of the RETURNEDMET array requiring additional information to be stored for an appropriate re-binning. To avoid this problem, as explained in Section 3.2.2, we have simply kept the RETURNEDMET fixed in cosmic time between two subsequent snapshots, and re-binned it only when the present time coincides with the cosmic time corresponding to a snapshot.

This paper has been typeset from a TEX/LATEX file prepared by the author.